Volume 3, Issue 3, 2017

Journal of Biomedical Photonics & Engineering

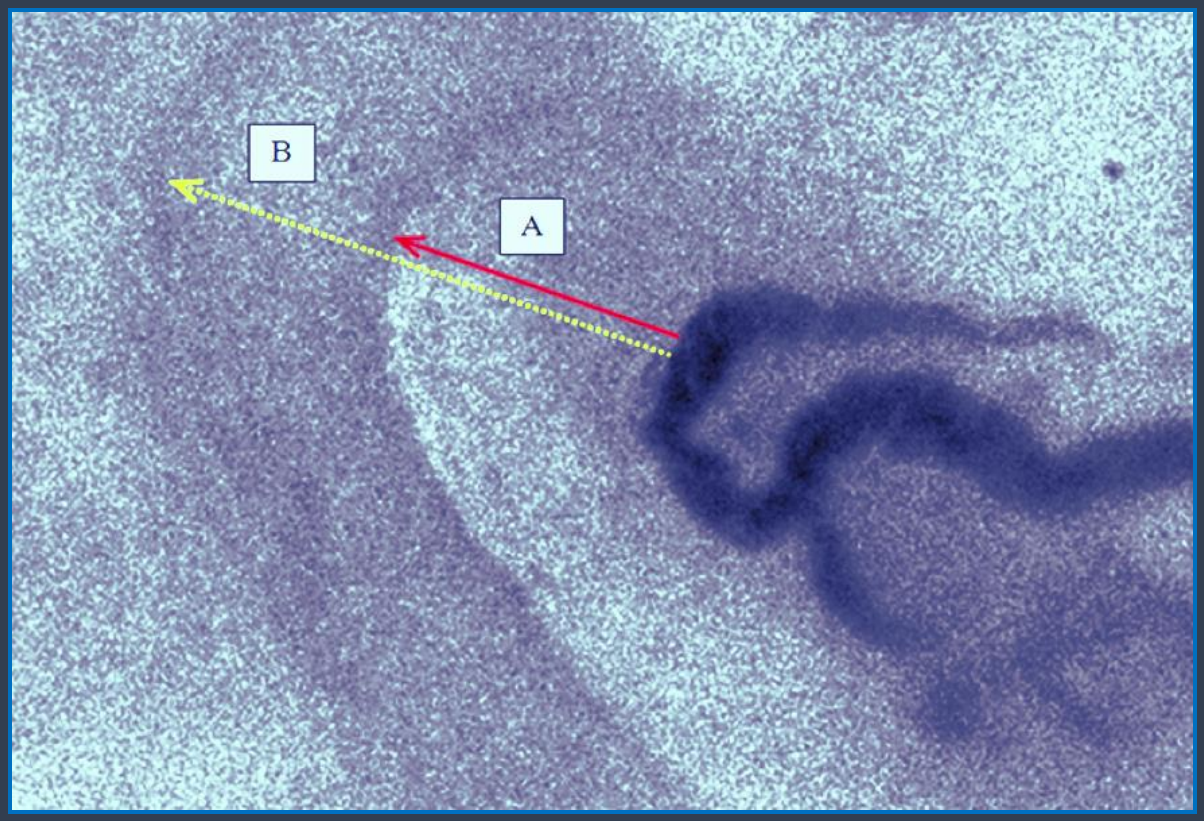

 doi: 10.18287/JBPE17.03.030001

Journal of Biomedical Photonics & Engineering

by Samara National Research University

Volume 3, Issue 3 (September 2017)

Editorial Board

Used Figure from this issue on the Cover

Yury I. Gurfinkel, et al. Potentialities of Digital Capillaroscopy in the Diagnostics of Oedema Syndrome, 030401, Fig. 1 (colorized).

Postal address:

39B Lukacheva st., room #301

Samara 443086, Russian Federation

Contents

The Characteristics of Brain Structural Network in Patients with Low Grade Glioma Revealed by Diffusion Tensor Imaging

Ling Tao[1]*, Zhiyu Qian[1], Yamin Yang[1], Hongyi Liu[2], and Li Xue[1]
[1]Nanjing University of Aeronautics and Astronautics, No.29, Yudao Street, Nanjing, 210016, China
[2]Nanjing Brain Hospital Affiliated to Nanjing Medical University, No.264, Guangzhou Road, Nanjing, 210029, China

***e-mail:** taoling@nuaa.edu.cn

Abstract. *Purpose:* At present, few studies have investigated the functional performance in patients with low grade glioma (LGG) from the perspective of brain structural characteristics. This study aimed to analyze the topological properties of brain structural networks in LGG patients and investigate the influence of operation and lesion location on whole-brain and hemisphere networks. On this basis, the structural plasticity and function compensatory mechanism of LGG patient were discussed. *Method*: We constructed whole-brain and hemisphere anatomical networks for 20 LGG patients and 20 normal controls (NC). The structural connections were established by selecting an appropriate connectivity threshold. Brain hub nodes and random nodes between LGG and NC were compared. Statistical analyses were performed to reveal the significant differences of various network characteristics between LGG patients and NC as well as between LGG patients before and after operation. The two-factor variance analysis was used to investigate the influence of operation and lesion location on whole-brain and hemisphere networks. *Results:* From the graph-based topological metrics of the constructed network, various global parameters changed significantly in LGG patients. Meanwhile, altered regions in the LGG patients was obtained and various nodal parameters were further calculated in each region. Most of hub nodes were identical between LGG and NC groups, while the betweenness centrality values of those hub nodes and some random nodes were higher in the LGG patients. By comparing LGG patients pre- and post- operation, more significantly altered network metrics were obtained from hemisphere network analysis than that from whole-brain network analysis, and network features of dominant hemisphere changed more drastically when the lesion is located in the same hemisphere. *Conclusion:* To conclude, the present study indicates the existence of compensatory mechanism in LGG patients to adapt to cognitive requirements. Function reorganization and the rewiring of neuronal circuits allow signal transmission bypassing the lesion area or surgical trauma. It also suggests that graph-based topological metrics analysis could become a useful method to provide valuable indices of brain function in the evaluation of the LGG. © 2017 Journal of Biomedical Photonics & Engineering.

Keywords: Structural network; Topological properties; Brain plasticity; Compensatory mechanism; Functional lateralization.

Paper #3154 received 24 Jan 2017; revised manuscript received 5 May 2017; accepted for publication 10 May 2017; published online 15 Jun 2017. doi: 10.18287/JBPE17.03.030301.

References

1. E. G. Shaw, B. W. Scheithauer, and J. R. OFallon, "Management of supratentorial low-grade gliomas," Seminars in Radiation Oncology 1(1), 23-31 (1993).
2. E. F. Chang, A. Clark, J. S. Smith, M.-Y. Polley, S. M. Chang, N. M. Barbaro, A. T. Parsa, M. W. McDermott, and M. S. Berger, "Functional mapping-guided resection of lowgrade gliomas in eloquent areas of the brain: improvement of long-term survival," Journal of Neurosurgery 114(3), 566-573 (2011).
3. J. R. Petrella, L. M. Shah, K. M. Harris, A. H. Friedman, T. M. George, J. H. Sampson, J. S. Pekala, and J. T. Voyvodic, "Preoperative functional MR imaging localization of language and motor areas: effect on therapeutic decision making in patients with potentially resectable brain tumors," Radiology 240(3), 793-802 (2006).
4. S. M. Smirnakis, M. C. Schmid, B. Weber, A. S. Tolias, M. Augath, and N. K. Logothetis, "Spatial specificity of BOLD versus cerebral blood volume fMRI for mapping cortical organization," Journal of Cerebral Blood Flow & Metabolism 27(6), 1248-1261 (2007).
5. A. G. Goloshevsky, C. W.-H. Wu, S. J. Dodd, and A. P. Koretsky, "Mapping cortical representations of the rodent forepaw and hindpaw with BOLD fMRI reveals two spatial boundaries," Neuroimage 57(2), 526-538 (2011).
6. C. M. Filley (ed.), The Behavioral Neurology of White Matter, Oxford University Press, New York (2001). ISBN: 978-0-1951-3561-9.
7. P. J. Basser, and D. K. Jones, "Diffusion-tensor MRI: theory, experimental design and data analysis – a technical review," NMR Biomed 15(7-8), 456–467 (2002).
8. E. Bullmore, and O. Sporns, "Complex brain networks: graph theoretical analysis of structural and functional systems," Nature Reviews Neuroscience 10(3), 186-198 (2009).
9. M. R. Del Bigio, M. J. Wilson, and T. Enno, "Chronic hydrocephalus in rats and humans: white matter loss and behavior changes," Ann Neurol 53(3), 337-346 (2003).
10. Y. Ding, J. P. McAllister, B. Yao, N. Yan, and A. I. Canady, "Axonal damage associated with enlargement of ventricles during hydrocephalus: a silver impregnation study," Neurol Res 23(6), 581-587 (2001).
11. M. Lazar, A. L. Alexander, P. J. Thottakara, B. Badie, and A. S. Field, "White matter reorganization after surgical resection of brain tumors and vascular malformations," American journal of neuroradiology 27(6), 1258-1271 (2006).
12. G. Gong, Y. He, L. Concha, C. Lebel, D. W. Gross, A. C. Evans, and C. Beaulieu, "Mapping anatomical connectivity patterns of human cerebral cortex using in vivo diffusion tensor imaging tractography," Cerebral cortex 19(3), 524-536 (2009).
13. B. Wang, Y. Fan, M. Lu, S. Li, Z. Song, X. Peng, R. Zhang, Q. Lin, Y. He, J. Wang, and R. Huang, "Brain anatomical networks in world class gymnasts: A DTI tractography study," NeuroImage 65, 476-487 (2013).
14. J. T. Duda, P. A. Cook, and J. C. Gee, "Reproducibility of graph metrics of human brain structural networks," Frontiers in Neuroinformatics 8(46), (2014).
15. M. Bastiani, N. J. Shah, R. Goebel, and A. Roebroeck, "Human cortical connectome reconstruction from diffusion weighted MRI: the effect of tractography algorithm," NeuroImage 62(3), 1732-1749 (2012).
16. C. Thomas, F. Q. Ye, M. O. Irfanoglu, P. Modi, K. S. Saleem, D. A. Leopold, and C. Pierpaoli, "Anatomical accuracy of brain connections derived from diffusion MRI tractography is inherently limited," Proceedings of the National Academy of Sciences 111(46), 16574-16579 (2014).
17. B. C. M. van Wijk, C. J. Stam, and A. Daffertshofer, "Comparing brain networks of different size and connectivity density using graph theory," PLoS One 5(10), e13701 (2010).
18. D. J. Watts, and S. H. Strogatz, "Collective dynamics of 'small-world' networks," Nature 393(6684), 440-442 (1998).
19. M. D. Humphries, and K. Gurney, "Network 'small-world-ness': a quantitative method for determining canonical network equivalence," PLoS One 3(4), e0002051 (2008).
20. O. Sporns, and J. D. Zwi, "The small world of the cerebral cortex," Neuroinformatics 2(2), 145-162 (2004).
21. R. Albert, and A. Barabási, "Statistical mechanics of complex networks," Reviews of modern physics 74(1), 47-97 (2002).
22. S. Achard, and E. Bullmore, "Efficiency and cost of economical brain functional networks," PLoS Comput Biol 3(2), e17 (2007).
23. L. C. Freeman, "A set of measures of centrality based on betweenness," Sociometry 40(1), 35-41 (1977).
24. V. Gol'dshtein, G. A. Koganov, and G. I. Surdutovich, "Vulnerability and hierarchy of complex networks," arXiv preprint, cond-mat/0409298 (2004).
25. P. Holme, B. J. Kim, C. N. Yoon, and S. K. Han, "Attack vulnerability of complex networks," Physical Review E 65(5), 1-15 (2002).
26. L. da F. Costa, F. A. Rodrigues, G. Travieso, and P. R. Villas Boas, "Characterization of complex networks: A survey of measurements," Advances in Physics 56(1), 167-242 (2007).

27. M. Girvan M, and M. E. J. Newman, "Community structure in social and biological networks," Proceedings of the National Academy of Sciences of the United States of America 99(12), 7821-7826 (2002).
28. V. Latora, and M. Marchiori, "Efficient behavior of small-world networks," Physical Review Letters 87(19), 1-4 (2001).
29. M. Filippi, and F. Agosta, "Magnetic resonance techniques to quantify tissue damage, tissue repair, and functional cortical reorganization in multiple sclerosis," Prog Brain Res 175, 465-482 (2009).
30. C. Sampaio-Baptista, A. A. Khrapitchev, S. Foxley, T. Schlagheck, J. Scholz, S. Jbabdi, G. C. DeLuca, K. L. Miller, A. Taylor, N. Thomas, J. Kleim, N. R. Sibson, D. Bannerman, and H. Johansen-Berg, "Motor skill learning induces changes in white matter microstructure and myelination, "J Neurosci 33(50), 19499-19503 (2013)
31. S. R. Wainwright, and L. A. M. Galea, "The Neural Plasticity Theory of Depression: Assessing the Roles of Adult Neurogenesis and PSA-NCAM within the Hippocampus," Neural Plasticity 2013, 1-14 (2013).
32. Healthline Medical Team, Frontal lobe, Medically Reviewed, 2 March 2015.
33. M. Macmillan, "Alfred walter campbell and the visual functions of the occipital cortex," Cortex 56, 157-181 (2014).
34. E. J. J. Habets, A. Kloet, R. Walchenbach, C. J. Vecht, M. Klein, and M. J. B. Taphoorn, "Tumour and surgery effects on cognitive functioning in high-grade glioma patients," Acta Neurochirurgica 156(8), 1451-1459 (2014).
35. M. Klein, H. Duffau, and P. C. D. W. Hamer, "Cognition and resective surgery for diffuse infiltrative glioma: an overview," Journal of neuro-oncology 108(2), 309-318 (2012).
36. K. Caeyenberghs, and A. Leemans, "Hemispheric lateralization of topological organization in structural brain networks," Human brain mapping 35(9), 4944-4957 (2014).
37. H. Cheng, Y. Wang, J. Sheng, W. G. Kronenberger, V. P. Mathews, T. A. Hummer, and A. J. Saykin, "Characteristics and variability of structural networks derived from diffusion tensor imaging," Neuroimage 61(4), 1153-1164 (2012).
38. D. K. Jones, T. R. Knosche, and R. Turner, "White matter integrity, fiber count, and other fallacies: the do's and don'ts of diffusion MRI," Neuroimage 73, 239-254 (2013).
H. Huang, N. Shu, V. Mishra, T. Jeon, L. Chalak, Z. J. Wang, N. Rollins, G. Gong, H. Cheng, Y. Peng, Q. Dong, and Y. He, "Development of Human Brain Structural Networks Through Infancy and Childhood," Cerebral Cortex 25(5), 1389-1404 (2015).

1 Introduction

Low-grade gliomas (LGGs) are a diverse group of gliomas that arise from uncontrolled growth of brain glial cells [1]. Surgical resection is considered as the primary option for the clinical treatment of LGG, with the aim of maximum tumor removal while preserving functional cortical and subcortical areas so as to minimize postoperative morbidities. The gold standard to identify the brain tumor margins and important brain regions is intraoperative electrophysiological cortical mapping (ECM), which has already been verified for its clinical application in maximizing tumor resection and significantly improving long-term survival in LGG patients [2]. However, intraoperative ECM often requires active participation and compliance of patients, high demands of technical expertise and is highly time and effort consuming.

In recent years, blood oxygenation level dependence functional MRI (BOLD-fMRI) has demonstrated its particular value in preoperative risk assessment in patients with LGG, which can facilitate planning of surgery, shorten the duration of the operation, and obtain prognostic information prior to surgery [3]. Nevertheless, BOLD-fMRI only provides information on cortical representation of brain function, but not on the course of the subcortical and deep white matter tracts [4, 5]. As the white matter possesses about 50% of the adult brain volume and consists of a complex array of neuronal fiber connectivity [6], brain lesions often affect the white matter and may alter the known anatomical path in which the fiber pass. Inadvertent transection may lead to equally devastating results as the resection of the eloquent cortex. As to LGG patients, functional impairment is not only originated from tumor areas, but also could be affected by damaged fiber bundles that connect tumor lesions with the rest of the brain. In order to assess the structural integrity and fiber orientation, diffusion tensor imaging (DTI) has been developed as a noninvasive MRI technique to provide information about the integrity and physiology of white matter fiber tracts and neural pathway connections [7].

Recently, network model has been proposed as a useful tool for investigating the structural organization and functional mechanisms of the human brain. Graph theoretical analysis can reveal key topological and geometrical properties of network such as small-worldness, modularity, and highly connected hubs, heterogeneous degree distributions, network information transfer efficiency and so on. Graph theoretical approaches can provide a new powerful way of quantifying the brain's structural and functional systems, identifying the alteration of brain activation and localizing corresponding functional regions in patients [8]. In contrast to the large number of studies

on functional network regarding other brain diseases, there are only a handful of reports on examining the function areas from the perspective of the cerebral anatomical network, and little is known about the alteration of the white matter fiber connection patterns in LGG patients.

Permanent damage to white matter integrity is known to occur in cases of severe and chronic exposure to mechanical intra-cranial pressure as happens in hydrocephalus [9, 10]. In case of LGG, the lesion mostly causes the fiber displacement or temporary damage which may result in substantial reorganization of the functional areas and could be recovered after operation [11]. Therefore, understanding the characteristics of brain anatomical network in LGG patients and how structural changes may affect the functional integration and interaction between different regions is very necessary for presurgical planning and evaluation of surgical treatments.

In present study, we constructed the whole brain and hemisphere anatomical networks for 20 brain LGG patients and 20 healthy subjects based on DTI technique, and then various graph theoretical analysis approaches were applied to examine the topological properties of brain network. Statistical analysis was performed to determine group differences in global and nodal properties between LGG patients and normal controls as well as between pre-surgery patients and post-surgery patients. Furthermore, the two-factor variance analysis was used to investigate whether the surgical treatment has an influence on hemisphere networks and whether the topological properties of hemisphere networks would change significantly when the lesion located in different brain hemisphere. The possible change of white matter plasticity and brain functional lateralization were discussed based on above results.

2 Methods and Materials

2.1 Subjects

This study included 20 LGG patients (10 males; mean age 51 years; range 16-67 years) and 20 healthy adult subjects (10 males; mean age 25 years; range 24-34 years). All patients with LGG were selected from Nanjing Brain Hospital, among which 12 cases of lesions are in the right hemisphere and 8 cases of lesions are in the left hemisphere. All LGG patients were diagnosed as frontal lobe or temporal lobe tumor, and the histopathological diagnosis was performed according to the WHO Classification of tumors affecting the central nervous system. All healthy subjects as the normal controls (NC) were recruited from voluntary participants in university. All participants were right-handed and had no history of neurological or psychiatric disease or head injury. All LGG patients received clinical cognitive function assessment pre-operation and post-operation, and had no significant cognitive dysfunction. Each participant was provided with a written informed consent before DTI examinations and this study was approved by the Medical Research Ethics Committee of Nanjing Brain Hospital.

2.2 Image acquisition

DTI was performed with a 3T Siemens Trio MR system with a 32-channel phased-array head coil. Head motion was minimized with restraining foam pads provided by the manufacturer. DTI data were acquired by employing a single-shot twice-refocused echo planar imaging (EPI) sequence in alignment with the anterior-posterior commissural plane. The parameters used for diffusion data acquisition were as follows: repetition time (TR) = 6, 500 ms, echo time (TE) = 95 ms, 30 non-linear diffusion directions with b = 1000 s/mm^2 and an additional volume with b = 0 s/mm^2, acquisition matrix = 128×128, field of view (FOV) = 240 mm × 240 mm, bandwidth (BW) = 1447 Hz/pixel. 3D high-resolution brain structural images (voxel size = 1 mm^3, isotropic) were acquired using a T1-weighted magnetization-prepared rapid gradient-echo (MP-RAGE) sequence for each subject. The sequence parameters: TR/TE = 1900 ms/2.49 ms, inversion time (TI) = 900 ms, flip angle (FA) = 9°, FOV = 250 mm × 250 mm, and 176 sagittal slices covering the whole brain. For each subject, both the DTI data and the brain structural images were acquired in the same session.

2.3 Data preprocessing and network construction

Firstly, the cerebrum was automatically partitioned into 90 cortical and subcortical regionals (45 for each hemisphere) according to the widely accepted Automated Anatomical Labeling (AAL) atlas [12]. Since this atlas only has T1-weighted structural images, the DTI image cannot be directly registered to the AAL atlas. Therefore, inverse transformations were used to warp the AAL atlas from the Montreal Neurological Institute (MNI) space to the DTI native space in which the discrete labeling values were preserved by using a nearest neighbor interpolation method [12, 13]. Briefly, for each subject, the individual T1-weighted images were firstly coregistered to the b0 images in the native diffusion space using a linear transformation. The transformed T1 images were then nonlinearly transformed to the ICBM152 T1 template in MNI space. The above linear and nonlinear transformations were all performed using the SPM8 package (http://www.fil.ion.ucl.ac.uk/spm/software/spm8). Using this procedure, we obtained 90 cortical and subcortical region of interest (ROIs), each representing a node of the network.

Next, the fibers linking each pair of brain regions in the diffusion space were reconstructed. The whole-brain fiber tracking was constructed using DTI studio2.4 software (http://www.mristudio.org) based on the Fiber Assignment by Continuous Tracking (FACT) algorithm. Fiber tracking was stopped at voxels where FA < 0.2 or

if the turning angle between two eigenvectors of two consecutive voxels was greater than 45° [13].

To define the network edges, we selected a threshold value of three fibers to ensure that the average size of the biggest connected component of the network keeps 90 across all subjects (threshold selection will be introduced in details in section 2.4). That is to say, if there are at least three fibers with end points in regions u and v , then the two nodes u and v are connected with an edge. And the number of fibers between regions was only used to indicate the existence/absence of the edge. In this way, the binarized anatomical network for each subject was constructed and represented by a symmetric 90 × 90 matrix.

The construction process of anatomical networks is illustrated in Fig. 1. Firstly, AAL atlas in DTI native space (Fig. 1 (a)) was used to segment the whole-brain fiber tracking results (Fig. 1 (b)) into 90 regions. Then, fiber number in each region was extracted, and a 90 × 90 binary matrix (Fig. 1 (c)) was obtained by setting a threshold value of fiber number. Next, according to the symmetric 90 × 90 matrix, we can extract two 45 ×45 binary matrix representing the structural connectivity of left and right hemisphere, respectively (Fig. 1 (e) and (f)). The visualization of brain networks (Fig. 1 (d), (g) and (h)) were obtained using Brainnet software (http://www.nitrc.org/projects/bnv/).

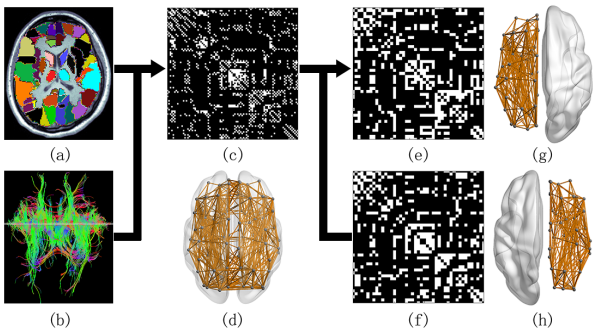

Fig. 1 Schematic illustration of the construction process of structural networks by DTI. (a) The AAL atlas was warped from the MNI space to the DTI native space by using inverse transformations, obtaining the parcellation of the cortex into 90 brain regions for each subject. (b) The whole-brain fiber tracts were reconstructed by using deterministic fiber tractography. (c) A 90 × 90 binary matrix was obtained by extracting fiber number in each region. (d) The visualization of whole-brain anatomical network. A 45 × 45 binary matrix representing the structural connectivity of (e) left and (f) right hemisphere. The visualization of (g) left and (h) right hemisphere anatomical network.

2.4 Threshold selecting

During brain network construction, the network matrix threshold (τ) is critical, and the optimal value of τ would result in the most accurate reconstruction of networks [14]. Brain networks, as well as their topological properties, are often sensitive to the connectivity threshold [15-16]. If threshold τ is too low, the resulting network would include connections that do not actually exist in reality and vice versa. Even a small number of spurious or misdetected edges can affect the properties of networks to a large extent [17]. In our study, we determined the optimal threshold value based on the small-world characteristics of network. The concept of small-world was originally proposed by Watts and Strogatz [18]. The small-world properties of a network can be characterized by the normalized clustering coefficient (γ) and the normalized characteristic path length (λ) of the network. These two conditions can be summarized into a scalar quantitative measurement, small-worldness, $\sigma = \gamma/\lambda$, which is typically larger than 1 for small-world networks [18, 19]. Many studies revealed that human brain has a typical small-world topology, which is characterized by large clustering coefficients and short mean path length [18, 20].

In this study, we evaluated the effects of different network matrix thresholds on the small world characteristics by setting the number of fiber bundles ranged from 1 to 5 (Fig. 2). We found that small worldness reached maximum when the fiber number was set to be 3, and thus the threshold of 3 fibers was used for anatomical networks construction in Section 2.3.

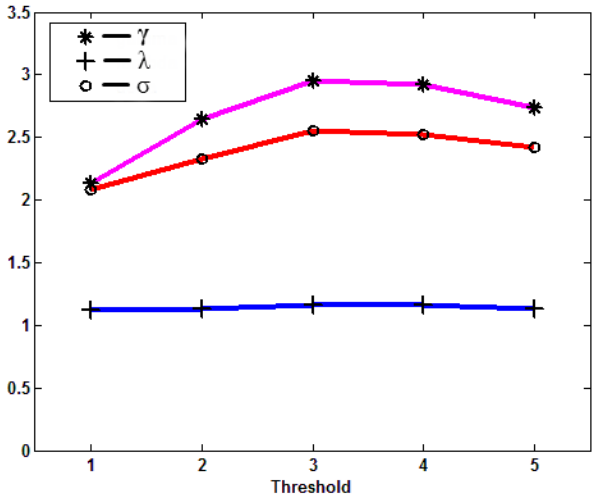

Fig. 2 Small world parameters under different threshold.

2.5 Network Analysis

The topological properties of anatomical networks were investigated at the global and regional (nodal) levels, respectively. The global properties of the whole brain networks were quantified in terms of clustering coefficient (C_p), characteristic path length (L_p), degree (K_p), local efficiency (E_{loc}) and global efficiency (E_{glob}) [19-20]. The regional properties were investigated by analyzing degree (K_i), clustering coefficient (C_i), shortest path length (L_i), local efficiency (E_{i_local}), regional efficiency (E_{nodal}),

normalized betweenness centrality (b_i) and vulnerability (V_i) of the node i [21-24]. Based on the constructed anatomical network of each subject, significant differences in global and the nodal properties between LGG patient and NC group were further studied.

As an important parameter of network evaluation, betweenness centrality is often used to assess the hub nodes in complex networks. The node with higher betweenness centrality value often exists in the concentrated areas with shortest path length, which means that more information will pass through and converge at this node. In this study, we calculated the value of betweenness centrality of 90 regions, and the averaged value of each region in all 20 subjects within the same group.

The vulnerability of the network can also be used to quantitatively assess the damage on network performance caused by a simulated failure of its element, *e.g.* removal of a particular node [24]. If one wants to protect the network by guarding or by a temporary isolation of some nodes (edges), the most important nodes (edges), breaking of which makes the whole network malfunctioning, should be identified [25]. In our study, to calculate the vulnerability values (V_i) of each node and edge, we removed the nodes or edges one by one from the network and calculated the changes in global efficiency of resulting network by: $V_i = (E_{glob} - E'_{glob}) / E_{glob}$. Where E'_{glob} is the global efficiency after the removal of the node i and all its edges [26].

2.6 Statistical analysis

Based on the binary network construction result in each subject, between-group differences (NC and LGG groups) in the graph-based metrics (global parameters C_p, L_p, K_p, E_{loc}, E_{glob}, γ, λ, and σ) of the anatomical networks were tested by two-sample t-tests. A two-sample two-tailed t-test was used to detect the relationship between nodal properties in network metrics with significant group difference, and a paired-samples t test was used to detect statistical difference between pre-operation and post-operation groups.

3 Results

3.1 Altered topological properties of anatomical networks in LGG patients

From the graph-based topological metrics of the constructed network, various global parameters (C_p, L_p, K_p, E_{loc}, E_{glob}, γ, λ, and σ) were calculated in all three groups, *i.e.* NC, pre-operation LGG and post-operation LGG group, and between-group statistical comparison was performed to detect significant difference, respectively. As shown in Table 1-3, all of three groups have similar path lengths ($\lambda \approx 1$) and high local clustering coefficients ($\gamma >> 1$), exhibiting typical small-world features.

Statistical analysis indicated that, compared with NC group, there is a significant increase in normalized clustering coefficient (γ) (p = 0.037 and p = 0.036), small-worldness (σ) (p = 0.043 and p = 0.040), and characteristic path length (L_p) (p = 0.037 and p = 0.035) in the anatomical networks of LGG patients (both pre-operation and post-operation), while a significant lower degree (K_p) (p = 0.022 and p = 0.025) and global efficiency (E_{glob}) (p = 0.030 and p = 0.032) were found in LGG patients. In addition, aside from the characteristic path length (L_p) (p = 0.048), there is no significant statistical difference in most of topological metrics of the whole-brain network in LGG patients pre- and post-operation. Therefore, following analysis of whole-brain topological properties will only be performed between NC and pre-operation LGG groups. As to the post-operation LGG group, the corresponding effects on the network properties upon surgical treatments will be discussed in details by deciphering the topological metrics of hemisphere networks.

Table 1 The comparison of topological properties between NC and pre-operation LGG groups.

	γ*	λ	σ*	CP	LP*	KP*	Eglob*	Eloc
NC	2.6837	1.1422	2.3496	0.4953	2.3115	12.8706	0.5022	0.7452
LGG(pre-)	2.8472	1.1531	2.4692	0.4950	2.3801	11.9356	0.4871	0.7434

*Significant group differences at p<0.05

Table 2 The comparison of topological properties between NC and post-operation LGG groups.

	γ*	λ	σ*	CP	LP*	KP*	Eglob*	Eloc
NC	2.6837	1.1422	2.3496	0.4953	2.3115	12.8706	0.5022	0.7452
LGG(post-)	2.8511	1.1536	2.4712	0.4951	2.4212	11.8701	0.4827	0.7473

*Significant group differences at p<0.05.

Table 3 The comparison of topological properties between pre- and post-operation LGG groups.

	γ	λ	σ	CP	LP*	KP	Eglob	Eloc
LGG(pre-)	2.8472	1.1531	2.4692	0.4950	2.3801	11.9356	0.4871	0.7434
LGG(post-)	2.8511	1.1536	2.4712	0.4951	2.4212	11.8701	0.4827	0.7473

*Significant group differences at $p<0.05$

.

3.2 Alteration of hub nodes in patients

Betweenness centrality and vulnerability were used to define network hub nodes. Firstly, the average betweenness centrality and vulnerability of each node in NC and LGG groups were calculated, respectively. As shown in Fig.3, the betweenness centrality values of 90 brain regions were sorted in descending order for NC group, and the betweenness centrality values for LGG groups and the vulnerability values for both two groups were sorted accordingly. On the whole, the changes of betweenness centrality values coincided with the changes of vulnerability values in corresponding groups. As the betweenness centrality of nodes are closely related to the network performance, and the removal of nodes with higher betweenness centrality would result in possible damage of network, *i.e.* the increase of vulnerability values. Consistent with previous studies, nodes with higher betweenness centrality value are thus identified as hub nodes in our study [23, 27]. More specifically, a node was defined as hub node if its betweenness centrality value is at least one standard deviation above the network mean. Thirteen hub nodes were determined in NC group, among which 9 hub nodes locating in associative cortex, 2 hub nodes locating in paralimbic cortex, and 2 hub nodes locating in subcortical region. In LGG group, 10 hub nodes were identified, including 5 hub nodes in associative cortex, 3 hub nodes in paralimbic cortex, and 2 hub nodes in subcortical region.

In order to visualize the location of hub nodes, 3D distribution diagram of hub nodes was obtained (Fig. 4). Clearly, most of the hub nodes were identical and distributed in same location (with color-coded in red) in both NC and LGG group, while 3 hub regions only existed in the NC group (middle part in Fig. 4, color-coded in green), *i.e.* left superior frontal gyrus-dorsolateral (SFGdor.L), left superior occipital gyrus (SOG.L) and left Lingual gyrus (LING.L)In order to show the similarities in the spatial patterns of the node betweenness of the two groups, we plotted the correlation-degree of the betweenness centrality of all 90 regions in the anatomical networks of the NC and LGG groups. As shown in Fig. 4 (right), red dots represent hub regions that exist in both groups, green dots refer to the 3 hub regions specific to the NC group, and pink circles represent those nodes that are not identified as hub nodes. From our results, the non-hub nodes (random nodes) showed the best correlation between the two groups ($r = 0.8907, p = 7.13e-32$), which means the majority of structural networks may remain relatively stable in LGG group. On the other hand, some random nodes with increased betweenness centrality values were found in LGG group, which could contribute to the alteration of brain functional network.

3.3 Alteration of network regional parameters in patients

The topological properties of anatomical networks were also investigated at regional (nodal) levels. Altered regions in the LGG patients was obtained and various nodal parameters were further calculated in each region. Two-sample two-tailed t-test was performed to determine group difference in the nodal properties between the NC and LGG groups. Three significance thresholds of $p < 0.05$, 0.01, and 0.005 was used for testing each of the graph-based metrics, respectively. As shown in Fig. 5, compared with NC group, significant decrease of degree (K_i) and regional efficiency (E_{nodal}) were found in LGG group in various regions, especially in the frontal (ORBsupmed.L, ORBinf.L, ORBsup.L, SFGdor.L), occipital (SOG.R), supplementary motor areas (SMA.L, SMA.R) and median cingulate and paracingulate gyri (DCG). On the contrary, path length (L_i) increased significantly in the frontal and occipital regions, while demonstrating opposite changes in the supplementary motor areas and median cingulate and paracingulate gyri. The clustering coefficient (C_i) and local efficiency (E_{i_local}) showed a significant decrease in the middle frontal gyrus (ORBmid.L) and a significant increase in the olfactory cortex (OLF) in LGG patients.

3.4 Altered topological properties of hemisphere networks in patients

In order to investigate whether the topological properties of hemisphere networks (lesion side) would have significant changes when the lesion located in different brain hemisphere, and whether the operation (tumor removal) has an influence on hemisphere networks (lesion side), we performed the two-factor variance analysis with "Lesion location" and "surgery or not" as the fixed factors. Variance analysis results in Table 4 indicated that, surgery would result in significant changes in various parameters including K_p、L_p、E_{glob}, while the lesion location in different brain hemisphere would only cause significant difference in clustering coefficient(C_p).

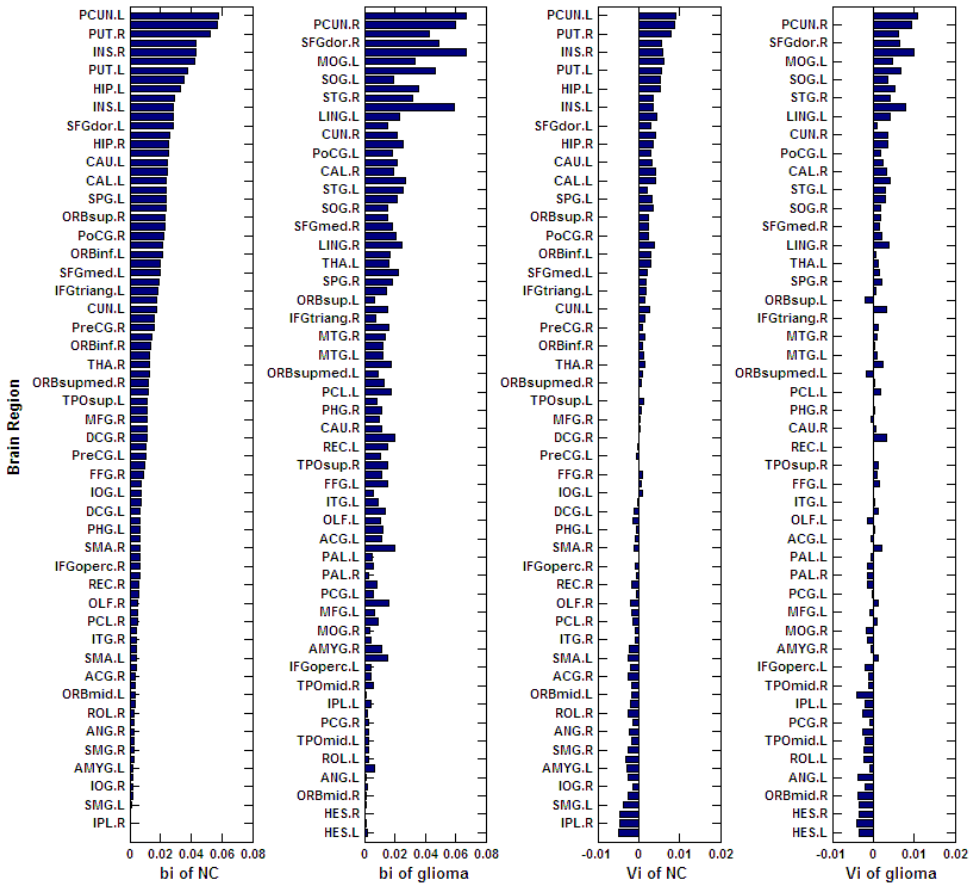

Fig. 3 Betweenness centrality (bi) and vulnerability (Vi) values of corresponding brain regions in NC and LGG groups.

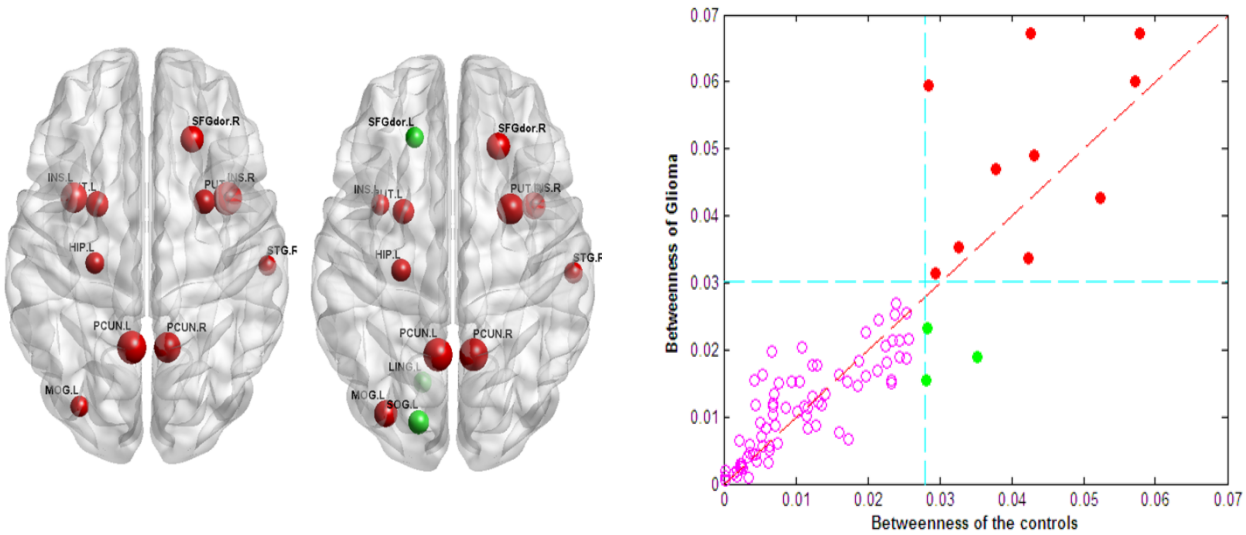

Fig. 4 Hub nodes distribution and correlation degree of all nodes between NC and LGG groups. From left to right: hub nodes distribution in LGG group; hub nodes distribution in NC group; the correlation-degree of betweenness centrality of all nodes between two groups. The size of the node represents the magnitude of the betweenness centrality. Nodes color-coded in red represent hub regions detected in the anatomical networks of both the subject groups. Nodes color-coded in green represent hub regions specific to the controls. The location of the regions was visualized with the BrainNet View software (http://www.nitrc.org/projects/bnv).

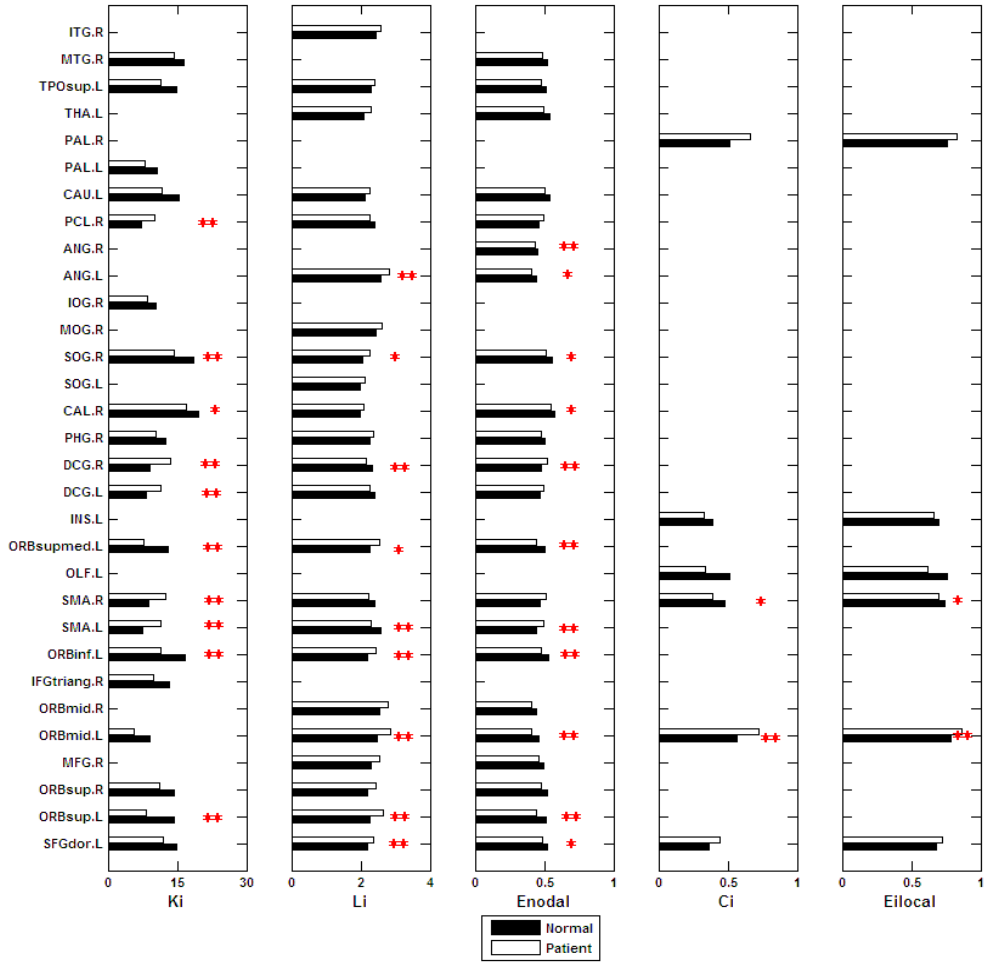

Fig. 5 Distribution of regions with significantly altered nodal properties in NC and LGG groups. Unstarred bars: significance with p<0.05; *:p<0.01; **:p<0.005.

Table 4 The results of variance analysis with “Lesion location” and “surgery or not” as the fixed factors.

		K_p	C_p	L_p	E_{glob}	E_{local}	γ	λ	σ
Lesion(left/right)	F	0.559	4.189	0.027	0.153	3.521	1.215	0.112	1.531
	P	0.350	0.040*	0.917	0.712	0.083	0.282	0.751	0.233
Surgery(pre-/post-)	F	5.287	0.128	5.512	5.519	0.076	2.899	2.181	2.745
	P	0.023*	0.744	0.026*	0.021*	0.813	0.095	0.162	0.111

Note: Significant group differences at *p < 0.05

Table 5 The parameter comparison of hemisphere networks with significant difference.

	E_{glob}	$\frac{K_p}{E_{glob}}$	L_p	$pre-C_p$	$post-C_p$
Pre-	0.572	11.214	2.321	—	—
Post-	0.559	10.387	2.386	—	—
left	—	—	—	0.532	0.538
right	—	—	—	0.579	0.545

Note: Significant group differences at *p < 0.05

Comparing those network parameters （K_p、L_p、E_{glob}）with significant difference between pre-operation and post-operation groups, we found that the value of global efficiency (E_{glob}) and degree (K_p) decreased, while the characteristic path length (L_p) increased after surgery (Table 5). In addition, regardless of operation conditions, for the lesion in right hemisphere, the clustering coefficient (C_p) were always greater than that in left hemisphere.

4 Discussion

4.1 Altered topological properties of anatomical networks in patients

This study compared the global and regional properties of brain anatomical networks of LGG patients with those of healthy controls. Consistent with previous studies, we found that the anatomical networks of both the LGG patients (pre- and post-surgery) and the controls showed features of small-worldness, characterized by a high value of local clustering coefficients ($\gamma >> 1$) but low values of path lengths ($\lambda \approx 1$).

Based on the graph theoretical analysis results, a decrease in degree and global efficiency and an increase in path length were found in LGG group. As the degree of each node is closely related to the connectivity of anatomical network, a decreased degree in LGG patients could result in a sparser network as compared with NC group [19]. According to the definition of key metrics in graph theory, the decreased degree will increase the path length of signal flow, and will contribute to the decrease of global efficiency [28]. In good agreement with this, decreased global efficiency and increased path length were indeed found in LGG patients, which is suggestive of slow information transmission and inefficient communication between brain regions. Interestingly, our graph analysis also revealed changes in the small-world network architecture, with a significant increase in small-worldness and clustering coefficient in LGG patients. More prominent small world network organization was observed in LGG patients compared to healthy controls, which could be interpreted as a compensatory mechanism. Comparing LGG patients pre- and post- operation, there is no significant between-group difference in small-world characteristics despite an increased path length in post-surgery group. As the topological characteristics of whole-brain network remained almost stable regardless of surgery conditions, we speculate that local network properties could be better indicators for evaluating the surgical effectiveness and will discuss in details below.

4.2 Alteration of hub nodes in patients.

Compared with normal subjects, three hub nodes were missing in LGG patients: left superior frontal gyrus-dorsolateral (SFGdor.L), left superior occipital gyrus (SOG.L) and left Lingual gyrus (LING.L). SOG.L and LING.L are both located in the upper part of occipital lobe, and SFGdor.L is located in the middle-upper part of frontal gyrus, suggesting these brain regions could be more susceptible to LGG. The absence of these hub nodes indicates that the topological structure of functional networks was probably restrained by the lesions in LGG patients, and these regions could become less important for information transmission with the presence of LGG.

The distribution of other hub nodes, such as precuneus (PCUN), insula (INS), lenticular putamen (PUT), hippocampus (HIP), and the pillow back (MOG), are mostly identical between NC and LGG group. However, the betweenness centrality values of these hub nodes are higher in LGG group than those in NC, suggesting these hub nodes could be directly associated with structural and functional modifications and become more important in the anatomical network in LGG group. Most of the hub nodes tend to change towards a high betweenness centrality value (red dots in Fig. 4 right) in LGG patients, while the majority of random nodes (non-hub nodes) remained stable between two groups. Nevertheless, there exist some random nodes with high-betweenness value, and these nodes may play more active role in the network due to brain plasticity and functional modifications. When signals cannot directly flow through the shortest path between two hub nodes, it may flow through indirect connections of non-hub nodes [29, 30]. In the human brain network, evidence suggests that mechanisms of brain plasticity include the strengthening of specific connections or the recruitment of parallel and indirect connections [31]. Therefore, based on this mechanism, the rewiring of neuronal circuits and reorganization of tracts between the regions may occur in response to LGG, allowing signal transmission via longer paths bypassing the lesion area. Indeed, in our results, significantly increased average path length was found in the LGG group.

It also implies that, for presurgery planning, we cannot only focus on the hub nodes, and those random nodes with temporary function alteration and neural reconnection capabilities may also play critical roles in the anatomical network. We therefore further investigated the function alteration by analyzing regional parameters of anatomical networks.

4.3 Alteration of network regional parameters in patients

Based on the analysis results of regional parameters, the node degrees and node efficiency of the LGG patients showed a significant decrease, while the average path length demonstrated a significant increase in the frontal and occipital regions. Furthermore, the clustering coefficient and local efficiency of the LGG patients also have a significant decrease in the frontal region. These finds suggest that the frontal region could be severely

damaged, which can be mainly explained by the presence of LGG in the frontal lobe or temporal areas in the subjects. The function of the frontal lobe involves integrating voluntary movement, longer non-task based memories, and accessing information for analysis and judgment [32]. Theoretically, the changes of regional parameters could be indicative of corresponding functional impairment. However, in our study, all of LGG patients were reported with no obvious clinical cognitive deficits, and we thus hypothesize that there may be some recovery on the basis of compensation mechanism as well as the participation of other regions to assume the lost functions of damaged areas. As the occipital regions are mainly responsible for visual functions [33], great alteration of nodal parameters found in occipital regions is consistent with clinical reports of vision loss in LGG patients. In addition, there were a significant increase of clustering coefficient and local efficiency in the supplementary motor area (SMA) and median cingulate and paracingulate gyri (DCG) in LGG patients, which indicated that these two regions might have more connections with other brain regions and play emerging roles in information signal transfer. In fact, SMA and DCG were not determined as hub nodes, but they could become more important during functional compensation due to brain structural plasticity. Together with above random nodes analysis results, in the presence of LGG lesions, function reorganization could exist with involvement of random nodes. During presurgical planning, while special attention should be paid into more accurate identification of the few highly influential nodes, the functions of those non-highly influential nodes (non-hub nodes) should never be underestimated. A throughout analysis of the regional parameters of brain network would help us to determine the critical nodal areas which could be related to possible functional impairment, so as to avoid unwanted damage during surgery and preserve the brain function to the maximum extent.

4.4 Altered topological properties of hemisphere networks in the patients

By comparing the topological properties of whole-brain network in LGG patients before and after operation, characteristic path length is the only parameter that changed significantly. In contrast, the hemisphere network metrics showed a great dependence on the operation, and the degree, global efficiency and the shortest path greatly altered with significant difference between pre- and post-surgery patients. We thus assume that local damage caused by operation could contribute to the altered network properties of affected brain hemisphere, while the whole-brain function could be compensated due to possible tracts reorganization and self-repairing mechanism.

Previous researches have showed that cognitive impairment may have significant difference when the lesion is located on different brain hemispheres. Compared with patients with gliomas located in non-dominant hemisphere, the patients with gliomas located in the advantage hemisphere usually had more severe cognitive impairment [34]. Moreover, resections of dominant temporal lobe were reported to be correlated with verbal memory decline, whereas non-dominant temporal lobe resections were associated with visuospatial memory decline [35]. From our results, the clustering coefficient showed a great dependence on the lesion location. As all of our subjects are right-handed and the left hemisphere is usually considered as the dominant hemisphere, brain network features of left hemisphere could be more sensitive to lesion sites and surgical trauma, which can be explained by the smaller cluster coefficient found in the group with lesion in left hemisphere. The asymmetry characteristics of brain network in healthy individual is associated with cognitive differences between left and right hemisphere [36]. Clearly, studies regarding network topological properties of hemispheres could bring more insights in understanding the lesion location-related brain cognitive damage and provide more knowledge for the evaluation of surgical treatment.

4.5 Methodological issues

Several methodological issues related to present study are discussed below. Firstly, in consideration of its simplicity, robustness and speed, and for better comparison with other previously reported studies [37], the commonly used deterministic tractography algorithm was applied to track fiber in our study. Noticed that this method cannot resolve crossing fiber bundles [38], future study using probabilistic tractography [39] could be an alternative approach to address this issue. Secondly, there is actually no physiological criterion for definition edge and node selection in human brain anatomical network construction. Similar to other studies [12-13], we used the AAL template and fiber number to determine nodes and edges, respectively. However, as the nodes and edges are closely related to the substantial analysis results of the constructed network, their physiological definition could be of great importance and requires future studies supported by a wealth of evidence from both anatomical and physiological studies. At last, as a pilot proof-of-concept study, the results obtained in our studies were based on a relatively small sample size. We believe that more comprehensive investigation towards a more precise data interpretation could be achieved with continuous expanding of sample size.

5 Conclusion

In this paper, we constructed the anatomical networks of whole-brain and hemisphere in NC, pre-surgery and post-surgery LGG patient groups, then the topological properties and regional parameters of networks were analyzed and compared, respectively. Our results showed that the presence of lesion and operation may alter the information transmission path between regions,

making original direct signal transmission through hub nodes turn into indirect signal transmission through non-hub nodes, characterized by the increase of path length. At the same time, more prominent small world network organization in LGG patients can evidence the active processes of neuroplasticity and compensatory mechanism in response to the presence of LGG. In addition, due to possible tract reorganization and network reconfiguration, some non-highly influential nodes became progressively important with the presence of lesion or in response to operation, of which functions cannot be underestimated. It is thus necessary to investigate those nodal regions by further analyzing regional parameters of network. Comparing the whole-brain and hemisphere anatomical networks of LGG patients pre- and post- operation, whole-brain function in post-operation LGG patients could be compensated as a result of self-repairing mechanism, while hemisphere network metrics changed significantly before and after operation, suggesting that hemisphere-dependent network analysis could bring valuable information for the evaluation of treatment effectiveness. Furthermore, it is found that brain network metrics altered more significantly when the lesion is located in the dominate hemisphere. This finding could be helpful for understanding the cognitive function related to lesion location and provide a new way to predict and evaluate the effects of surgical treatments.

Acknowledgments

This work was supported by the Natural Science Foundation of China (Grant numbers: 61075107, 81601532), Natural Science Foundation of Jiangsu Province (BK20160814), and the Clinical medical science Special Foundation in Jiangsu Province (Grant numbers: SBL201230215), and Scientific Research Foundation of Nanjing University of Aeronautics and Astronautics (1003-YAH16009). Ling Tao would also like to thank China Scholarship Council awarding me a scholarship to pursue study in Monash University as a visiting scholar.

Confliance with ethical standards

Conflict of interes

Ling Tao, Zhiyu Qian, Yamin Yang, Hongyi Liu, Li Xue declare that they have no conflict of interest.

Ethical standard

All procedures were followed in accordance with the ethical standards of the responsible committee on human experimentation (institutional and national) and with Declaration of the Helsinki 1975, as revised in 2008 (5).

Informed consent

Informed consent was obtained from all patients for being included in the study.

Refractive Index Anisotropy and Diffusion Rate in Cartilage Tissue

Georgy V. Simonenko
N. G. Chernyshevsky Saratov National Research State University, 83 Astrakhanskaya str., Saratov 410012, Russia
e-mail: gvsim1960@hotmail.com

Abstract. The paper presents the results of experimental and theoretical studies of cartilage tissue optical characteristics after the immersion impact and without it. We have found that the immersion effect leads to structural changes in the cartilage tissue, in particular, to the increased size of the scattering elements. The refractive index anisotropy of the cartilage tissue is measured in the samples subjected to immersion impact and without it. We demonstrate theoretically that the diffusion kinetics of the immersion fluid in the biotissue strongly depends upon the anisotropy of the diffusion rate along the collagen fibres and in the perpendicular direction. Due to the diffusion anisotropy, the increase of the mean rate of the immersion fluid diffusion in the biotissue can lead to the fall of light transmission through the sample rather than to its expected increase.

Keywords: optical properties; cartilage tissue; diffusion; immersion clearing.

Paper #3224 received 21 Jun 2017; revised manuscript received 4 Sep 2017; accepted for publication 4 Sep 2017; published online 25 Sep 2017. doi: 10.18287/JBPE17.03.030302.

References

1. V. V. Tuchin, "Tissue optics and photonics: light-tissue interaction," Journal of Biomedical Photonics & Engineering 1(2), 98-134 (2015).
2. A. Bykov, T. Hautala, M. Kinnunen, A. Popov, S. Karhula, S. Saarakkala, M. T. Nieminen, V. Tuchin, and I. Meglinski, "Imaging of subchondral bone by optical coherence tomography upon optical clearing of articular cartilage," Journal of Biophotonics 9(3), 270-275 (2016).
3. V. V. Tuchin (Ed.), Coherent-Domain Optical Methods: Biomedical Diagnostics, Environmental Monitoring and Material Science, vol. 2, 2nd edition, Springer-Verlag, NY (2013).
4. S. M. Daly, and M. J. Leahy, "Go with the flow: a review of methods and advancements in blood flow imaging," Journal of Biophotonics 6(3), 217-255 (2013).
5. M. G. Ghosn, V. V. Tuchin, and K. V. Larin, "Non-destructive quantification of analytes diffusion in cornea and sclera by using optical coherence tomography," Investigative Opthalmology & Visual Science 48(6), 2726-2733 (2007).
6. E. A. Genina, A. N. Bashkatov, E. A. Kolesnikova, M. V. Basko, G. S. Terentyuk, and V. V. Tuchin, "Optical coherence tomography monitoring of enhanced skin optical clearing in rats *in vivo*," Journal of Biomedical Optics 19(2), 021109 (2013).
7. V. V. Tuchin, "Polarized light interaction with tissues," Journal of Biomedical Optics 21(7), 071114 (2016).
8. D. Zhu, K. V. Larin, Q. Luo, and V. V. Tuchin, "Recent progress in tissue optical clearing", Laser & Photonics Reviews 7(5), 732-757 (2013).
9. J. Wang, Y. Zhang, T. H. Xu, Q. M. Luo, and D. Zhu, "An innovative transparent cranial window based on skull optical clearing," Laser Physics Letters 9(6), 469-473 (2012).
10. E. A. Genina, A. N. Bashkatov, Yu. P. Sinichkin, I. Yu. Yanina, and V. V. Tuchin, "Optical clearing of biological tissues: prospects of application in medical diagnostics and phototherapy," Journal of Biomedical Photonics & Engineering 1(1), 22-58 (2015).
11. E. A. Genina, A. N. Bashkatov, M. D. Kozintseva, and V. V. Tuchin, "OCT study of optical clearing of muscle tissue in vitro with 40% glucose solution," Optics and Spectroscopy 120(1), 20-27 (2016).

12. C.-H. Liu, M. Singh, J. Li, Z. Han, C. Wu, S. Wang, R. Idugboe, R. Raghunathan, E. N. Sobol, V. V. Tuchin, M. Twa, and K. V. Larin, "Quantitative assessment of hyaline cartilage elasticity during optical clearing using optical coherence elastography," Modern Technologies in Medicine 7(1), 44-51 (2015).
13. E. A. Genina, A. N. Bashkatov, and V. V. Tuchin, "Tissue optical immersion clearing," Expert Review of Medical Devices 7(6), 825-842 (2010).
14. K. V. Larin, M. G. Goshn, A. N. Bashkatov, E. A. Genina, N. A. Trunina, and V. V. Tuchin, "Optical clearing for OCT image enhancement and in-depth monitoring of molecular diffusion," IEEE Journal of Selected Topics in Quantum Electronics 18(3), 1244-1259 (2012).
15. M. G. Ghosn, V. V. Tuchin, and K. V. Larin, "Depth-resolved monitoring of glucose diffusion in tissues by using optical coherence tomography," Optics Letters 31(15), 2314-2316 (2006).
16. O. I. Baum, A. I. Omel'chenko, I. O. Ryzhkov, M. V. Obrezkova, V. V. Lunin, and E. N. Sobol', "Effect of Omnipaque on the optical properties and laser-induced changes in the thermostability of nucleus pulposus of the intervertebral disk," Doklady Biochemistry and Biophysics 428, 261-263 (2009).
17. V. L. Vesnin, and V. G. Muradov "Spectrophotometric complex based on the monochromator MDR-41 for studying the absorption spectra in the range 400–1800 nm," Izvestiya Samarskogo nauchnogo tsentra Rossiiskoy Akademii Nauk 10(3), 724-731 (2008) [in Russian].
18. D. B. Judd, and G. Wyszecki, Color in Business, Science and Industry, 2nd ed., John Wily & Sons, NY (1975).
19. G. V. Simonenko, V. V. Tuchin, and N. A. Lakodina, "Measurement of the optical anisotropy of biological tissues with the use of a nematic liquid crystal cell," Journal of Optical Technology 67(6), 559-561 (2000).
20. V. Chigrinov, H. S. Kwok, D. Yakovlev, G. Simonenko, and V. Tsoi, "LCD optimization and modeling," Journal of the Society for Information Display 12(2), 183-187 (2004).
21. E. S. Bukareva, G. V. Simonenko, and V. V. Tuchin, "Features of the kinetics of the immersion clarification of biological tissue," Journal of Optical Technology 80(2), 119-123 (2013).
22. G. A. Korn, and T. M. Korn, Mathematical Handbook for Scientists and Engineers, McGraw-Hill. Book Co., New York (1968).
23. Yu. Ya. Kuzyakiv, K. A. Semenenko, and N. B. Zorov, Methods of Spectral Analysis, Izd-vo MGU, Moscow (1990) [in Russian].
24. D. A. Zimnyakov, G. V. Simonenko, and V. V. Tuchin, "Dispersion dependence of the optical anisotropy and the degree of depolarization of fibrous tissues," Journal of Optical Technology 77(9), 577-581 (2010).
25. K. V. Berezin, K. N. Dvoretskiy, M. L. Chernavina, V. V. Nechaev, A. M. Likhter, I. T. Shagautdinova, E. Yu. Stepanovich, O. N. Grechukhina, and V. V. Tuchin, "Studying the mechanism of tissue optical clearing using the method of molecular dynamics," Proc. SPIE 10336, 103360J (2017).
26. A. N. Bashkatov, E. A. Genina, T. G. Kamenskikh, et al., "Study of mildronate diffusion in th human eye sclera," Izvestiya Saratovskogo universiteta. Novaya seriya. Seriya Fizika 16(3), 167-177 (2016) [in Russian].
27. A. A. Ovchinnikov, S. F. Timashev, and A. A. Belyi, Kinetics of Diffusion-Controlled Chemical Processes, Khimiya, Moscow (1986) [in Russian].

1 Introduction

The diseases of musculoskeletal system, in which cartilage tissues are of particular importance, are widespread at present time. The arthrous cartilage is a biotissue playing a very important role in the normal functioning of joints, reducing the loads and providing the mobility. The condition of the cartilage tissue has to be determined for the diagnostics and treatment of various pathologies. At present, more and more optical diagnostic methods are used for this purpose. Optical diagnostics is promising because of its non-invasiveness, high functionality and high spatial resolution [1]. During the last decade the methods of optical coherence tomography (OCT) have been intensely developed and widely used in a number of applications [2, 3], including the visualisation of spatial distribution of blood vessels in human skin [4] and visualisation of molecular diffusion in biological tissues [5, 6]. For the diagnostics of cartilage tissue, the polarisation-sensitive OCT was used [7]. Essential enhancement of the OCT image contrast and increased probing depth can be achieved by applying the immersion clearing technique [8-11] to the studied samples, including those of the cartilage tissue [1, 12]. The principles of immersion clearing are based on the partial replacement of the interstitial fluid by an immersion agent and the partial tissue dehydration, which matches the refractive indices of collagen and interstitial fluid, as well as enhances the ordering of the tissue structural elements and, consequently, reduces the scattering of light by a biotissue [13-15]. As a rule, the random arrangement of the scattering structures in a biotissue causes fast depolarisation of the probing radiation. For this reason, many methods of optical diagnostics do not take the polarisation effects into account [5, 6, 8-11]. However, the polarisation effects can play a certain role in the probing of relatively thick samples of biotissue with polarised radiation, which can be characterised quantitatively by recording the degree of depolarisation of the transmitted light or the transformation of its initial polarisation state [7, 15]. Thus, the problem is how the anisotropy of a tissue (in

particular, cartilage) affects the diffusion kinetics of the tissue immersion clearing and how the immersion agent affects the biotissue structure and, therefore, the refractive index anisotropy. The latter can play an essential role in the development of polarisation-sensitive OCT [7]. The goal of the present paper is to determine the role of the tissue anisotropy in the kinetics of its immersion clearing and to estimate the structural changes of the tissue in this process. The study included the solution of the following problems: to estimate the effect of the immersion agent on the structure of the cartilage tissue, to estimate the cartilage refractive index anisotropy in the samples after immersion and the control ones, and to reveal the role of the diffusion rate anisotropy in the kinetics of the biotissue immersion clearing.

In the present paper, we report the results of studying the spectral characteristics (in the range from 400 to 1400 nm) and optical anisotropy properties of the cartilage tissue after the immersion clearing, as well as the kinetics of immersion agent diffusion in the cartilage with its anisotropy properties taken into account. The first part of the paper is devoted to the study of transmission spectra of the cartilage tissue affected by the immersion fluid and the determination of the cartilage refractive index anisotropy. The second part of the paper presents the results of computer simulation of the immersion fluid diffusion in the cartilage tissue with the structural anisotropy of the tissue taken into account.

2 Methods and materials

For the study, we used the samples of porcine ear cartilage. Before starting the experiment, the biotissue was cut into samples with the area of about 20 × 15 mm^2, in which the bundles of collagen fibres were parallel to the surface. Some samples were prepared from the right ear and some from the left ear of the same pig. The samples were divided into two groups, one of them subjected to the immersion with Omnipaque™ agent [16] by placing the biotissue sample into the liquid for a day. The second group was left intact for control. In each group, there were five samples. Then all samples were dried in air at the room temperature during three days to remove the free interstitial fluid from them. Before and after drying the thickness of the samples was measured with the accuracy of ±10 μm at a few points and then averaged. Before drying the mean thickness of the studied samples amounted to 2.3 ± 0.18 mm in the first group and 0.8 ± 0.05 mm in the second one. After drying the mean thickness of the studied samples was 1.5 ± 0.18 mm in the first group and 0.5 ± 0.05 mm in the second one. To improve the accuracy of the measurements, the thinner samples of the cartilage were used without immersion, and the thicker ones to study the consequences of immersion clearing. No additional processing of the samples was undertaken. The spectra of collimated transmission and the refractive index anisotropy of the biotissue samples were experimentally studied.

The transmission measurements were performed using the spectral system based on the MDR-41 monochromator, analogous to the system described in detail in Ref. [17]. As a radiation source, the halogen capsule lamp with the spectral range from 340 to 2500 nm was used. The transmission was measured with the spectral step of 1 nm. The limit resolution interval of the monochromator did not exceed 0.02 nm. The sample was illuminated with a parallel light beam 1 mm in diameter. Immediately after the sample the aperture having the diameter 1 mm was installed. The output slit of the monochromator was 10 μm wide and 2 mm high. The relative error of the transmission measurement did not exceed 1%. To obtain the transmission spectra the standard commercial MdrWin software operating under OS Windows and supplied together with the monochromator was used.

To measure the refractive index anisotropy, we used the method of visual colour determination (method A of Ref. [18]), based on the comparison of the etalon colour with the current colour of the sample. The relative error of this method does not exceed 2%. To analyse the polarised beam interference image colour in the biotissue samples, we used the polarised light microscope POLAM-P11 with 4× objective and digital camera DCM-500 connected to the computer. To determine the sample colour by the colour of the etalon we used the method of comparison, described in Ref. [19] and the software package MOUSE-LCD having the computation accuracy not worse than 5% [20]. The choice of the liquid crystal (LC) cell as an etalon is caused by the possibility of easy optical anisotropy variation of the liquid crystal by applying small electric voltage (from 0 to 10 V) to the control electrodes of the cell. In our case, a slightly modified technique of measuring the biotissue optical anisotropy was used, its main difference consisting in exploitation of a virtual LC cell. On the PC monitor, one window of any graphic editor displayed the image of the polarised beams interference, obtained by means of the polarised light microscope and the digital camera. The comparison window (etalon window) displayed the polarisation beams interference image in the virtual planar nematic liquid crystal cell. The virtual liquid crystal cell was simulated using the computer software MOUSE-LCD [20]. Given the thickness of the virtual LC cell d, the main physical parameters of the liquid crystal (Δn being the LC optical anisotropy), and the value of the control voltage on the cell electrodes, we calculated the value Δnd for the liquid crystal and the colour characteristics of the virtual cell. By changing the thickness of the liquid crystal layer, we achieved similar visual perception of the virtual liquid crystal cell image and the image of the biotissue sample. The similar visual perception of the etalon and sample was assumed to mean that the colour coordinated (i.e., the colour) of the sample and the etalon are similar, too. Since the change of the colour coordinates of the biotissue and the liquid crystal is caused only by the interference of polarised beams, for similar values of Δnd the transmission

spectra should be similar. Thus, we determined Δnd for the biotissue sample.

To study the kinetics anisotropy of the immersion fluid diffusion in the biotissue we used the method of computer simulation described in detail in Ref. [21]. Briefly, the essence of the method is the following. The problem of the immersion fluid diffusion in the biotissue sample is solved basing on the simple diffusion model, in which the difference of diffusion rates along the collagen fibres and in the perpendicular direction is taken into account. Let C be the concentration of the immersion fluid depending on the time t and three spatial coordinates x (inward), y (across the fibres and parallel to the surface) and z (along the fibres). The diffusion equation with three spatial coordinates has the form [21]:

$$\frac{\partial C(x,y,z,t)}{\partial t} = v_x(x,y,z)\frac{\partial^2 C(x,y,z,t)}{\partial x^2} + \\ +v_y(x,y,z)\frac{\partial^2 C(x,y,z,t)}{\partial y^2} + v_z(x,y,z)\frac{\partial^2 C(x,y,z,t)}{\partial z^2}, \quad (1)$$

where v_x, v_y, v_z are the immersion liquid diffusion rates along the respective coordinate axes.

Let the initial condition at $t = 0$ be specified in the form

$$C(x,y,z,0) = \varphi(x,y,z), \quad (2)$$

where $\varphi(x, y, z)$ is the surface distribution of the immersion fluid at the initial moment of time at the point of the clearing agent application.

In this model, the nonstationary, inhomogeneous, and anisotropic diffusion of the immersion fluid in the biotissue sample is considered. Assume that the immersion fluid can enter the sample from one side either all over the surface, or only in the centre of the sample, and the application domain has the shape of either a rectangle (the entire sample surface), or a circle with the uniform concentration. The biotissue is represented by a system of long cylindrical inclusions (collagen fibres), surrounded by the base substance. The characteristic geometric parameters of the inclusions are the length l_0, the diameter d_0, the separation a_0 between the inclusions along the axes x or y, the separation b_0 between the inclusions along the axis z, and the deviation angle φ between the inclusion and the z-axis, specified arbitrarily for each individual inclusion. The maximal possible deviation from the axis is an input parameter. To calculate the diffusion rate, we introduce the probability p that the diffusion at the considered point will go in a certain direction. Inside the collagen fibres, the probability is taken to be close to zero, since the collagen is much denser than the surrounding medium, and the molecular diffusion inside the fibres is hampered. If the considered point is in the base substance, and there is the base substance in the chosen direction, too, the diffusion probability is taken to be close to one. For each direction the coefficients of diffusion are recalculated at each point, namely, depending on the coordinate, the diffusion coefficient is multiplied by p. We solve Eq. (1) using the finite-difference method and the explicit scheme [22], assuming the diffusion rates along the x-axis and the y-axis constant or expressed in the known analytic form. For this purpose, we approximate the second derivatives in Eq. (1) by the ratios of finite differences, which yields the finite-difference equation:

$$\frac{c_{ijm}^{k+1} - c_{ijm}^{k}}{h_4} = v_x \frac{c_{i+1,jm}^{k} - 2c_{ijm}^{k} + c_{i-1,jm}^{k}}{h_1^2} + \\ +v_y \frac{c_{i,j+1,m}^{k} - 2c_{ijm}^{k} + c_{i,j-1,m}^{k}}{h_2^2} + \\ +v_z \frac{c_{ij,m+1}^{k} - 2c_{ijm}^{k} + c_{ij,m-1}^{k}}{h_3^2}, \quad (3)$$

where $x_i = ih_1$ ($i = 0,1,\ldots$), $y_i = jh_2$ ($j = 0,1,\ldots$), $z_m = jh_3$ ($m = 0,1,\ldots$), $t_k = kh_4$ ($k = 0,1,\ldots$), h_1 is the step in the direction Ox, h_2 is the step in the direction Oy, h_3 is the step in the direction Oz, and h_4 is the step in time t. The values of the grid function at the nodes (x_i, y_j, z_m, t_k) are denoted by the symbol c_{ijm}^{k}.

Eq. (3) can be written as a system of linear algebraic equations for the unknown values of the grid function in each layer.

In the zero layer the solution is found from the initial condition (2), presented as

$$c_{ijm}^{0} = \varphi(x_i, y_i, z_m). \quad (4)$$

Thus, solving the system of Eq. (3) with the initial conditions (4) we get the spatiotemporal dependence of the immersion fluid concentration in the sample. The described technique is implemented in the programme for calculating the kinetics of the fluid diffusion in the biotissue with the tissue anisotropy taken into account.

Below we present the results of experimental and computer studies of different properties of the cartilage tissue.

3 Optical properties of cartilage tissue

One of the simple and efficient ways to increase the probing depth and improve the quality of imaging the tissue internal structures is to reduce the light scattering by means of optical clearing agents [1-3]. The immersion optical clearing is based on the impregnation of the tissue with the biocompatible chemical agent possessing sufficiently high refractive index and hyperosmotic properties. Penetrating into the sample and interacting with the biotissue components, the agent reduces the refractive index difference between the scatterers and the surrounding base medium and changes the relative position and size of the tissue structural elements due to dehydration [10-13]. Thus, it

is possible to select three most probable mechanisms of the biotissue clearing, namely, the equalisation of refractive indices of the interstitial fluid and the collagen fibres, the change of collagen fibres packing density, and the size variation of the scatterers present in the biotissue. While the first mechanism is always present during the biotissue optical clearing, the second and the third ones require additional consideration. To eliminate the manifestations of the first mechanism, we dried all samples of the cartilage tissue before the measurements. Then we compared the optical characteristics (transmission spectra and refractive index anisotropy) of the samples subjected to the immersion before drying and the control samples, dried without immersion.

Fig. 1 presents the spectra of collimated transmission of the cartilage tissue samples after the immersion clearing and without it. For comparison, the transmission spectrum of the Omnipaque immersion agent itself is also shown. In the visible region, there is obviously no difference between the transmission spectra of the samples subjected to the immersion clearing and the control samples. In the infrared range, the observed situation is different. To analyse the spectra we used the differential spectroscopy method [23]. First, we see a different number of absorption peaks, the wavelengths of which are summarised in Table 1. The post-immersion cartilage tissue possesses six absorption peaks, while the intact tissue has only two peaks. The first absorption peak at 1000-1050 nm is nearly similar in all samples. The second peak in the samples subjected to the immersion manifests the own absorption Omnipaque agent. The common absorption peak at 1450-1500 nm is most probably due to the residual water. The rest three absorption peaks in the cartilage samples after immersion can be due to the structural changes of the biotissue induced by the immersing agent. Thus, the analysis of the transmission spectra shows that the application of immersion fluid changes the cartilage absorption spectrum in the infrared region and has no effect on the spectra in the visible range of optical radiation wavelengths. Therefore, the immersion fluid causes certain structural changes in the cartilage tissue.

Let us make some estimates of the cartilage tissue changes caused by the application of the immersion fluid. For these estimates, we chose the visible range, because in this range it is possible to perform independent polarisation measurements. For the measurements, we choose the transmission maximum for the samples with the immersion effect and without it. At the transmission maximum wavelength (873 nm) the ratio of scattering cross-section of the sample subjected to immersion σ_{im} and the control one σ_{wi} amounts to $\sigma_{im}/\sigma_{wi} = 1.083$. Since in the cartilage tissue the light is scattered by collagen fibres, the scattering cross-section is a function of the packing density f and diameter d_0 of the fibres. Thus, basing only on the transmission spectra of the cartilage tissue it is impossible to determine the changes produced in the biotissue by the immersion fluid. Therefore, we undertake independent measurements to answer this question.

To determine the refractive index anisotropy of the biotissue samples we exploited the polarised light microscope MIKMED, version 11. Using the method of colour comparison described above, we found that for the non-immersed sample $(\Delta n \cdot d) \approx 0.2$ μm and for the immersed one $(\Delta n \cdot d) \approx 0.6$ μm. Here Δn is the refractive index anisotropy in the biotissue and d is the sample thickness. Keeping in mind that the mean thickness was 1.5 mm for the immersed samples and 0.5 mm for non-immersed ones, we conclude that the in both cases the refractive index anisotropy is similar and amounts to nearly 0.0004. This value of the cartilage tissue anisotropy agrees with the data reported in [24]. Since in the cartilage tissue the refractive index anisotropy is caused by the shape anisotropy [1, 7, 24], which depends upon the refractive indices of the interstitial fluid and the collagen fibres, as well as upon the packing density of the collagen fibres f, we can conclude that the immersion fluid does not affect the collagen packing density. From the comparison of transmission spectra of immersed and non-immersed samples and the data on the refractive index anisotropy in such samples, we can draw a conclusion that the action of immersion fluid changes the size of the collagen fibres.

Now we can estimate the change of the collagen fibre size under the action of the immersion fluid on the cartilage tissue. Usually the model of a scattering medium, including the cartilage tissue, is considered to consist of cylinders with the length much greater than the diameter [2]. Since the packing density of the collagen fibres f is constant $\sigma_{im}/\sigma_{wi}=(d_{im}/d_{wi})^2$, d_{im} and d_{wi} being the collagen fibre diameter in the immersed sample and in the non-immersed one, respectively. It follows that $d_{im}/d_{wi} = 1.041$, i.e., the use of the immersion fluid increases the collagen fibre diameter by nearly 4%. The reliability of the obtained data is worth a brief separate discussion. The accuracy of the measurements is comparable with that for the refractive index anisotropy (the relative error of the visual colour determination method is 2%), and the accuracy of measuring the samples transmission spectra is essentially higher (the relative error does not exceed 1%). Since for the numerical estimation of the structural changes we used the data of spectral measurements, and the colour ones were used only to ascertain the fact that the refractive index anisotropy is constant (and, therefore, the packing density of the fibres is unchanged), the fact that the diameter of collagen fibres increases can be considered reliably established. Moreover, the increase of the collagen fibres diameter in the process of biotissue immersion clearing was reported by the authors of Ref. [25], in which using the methods of molecular dynamics it was shown that the

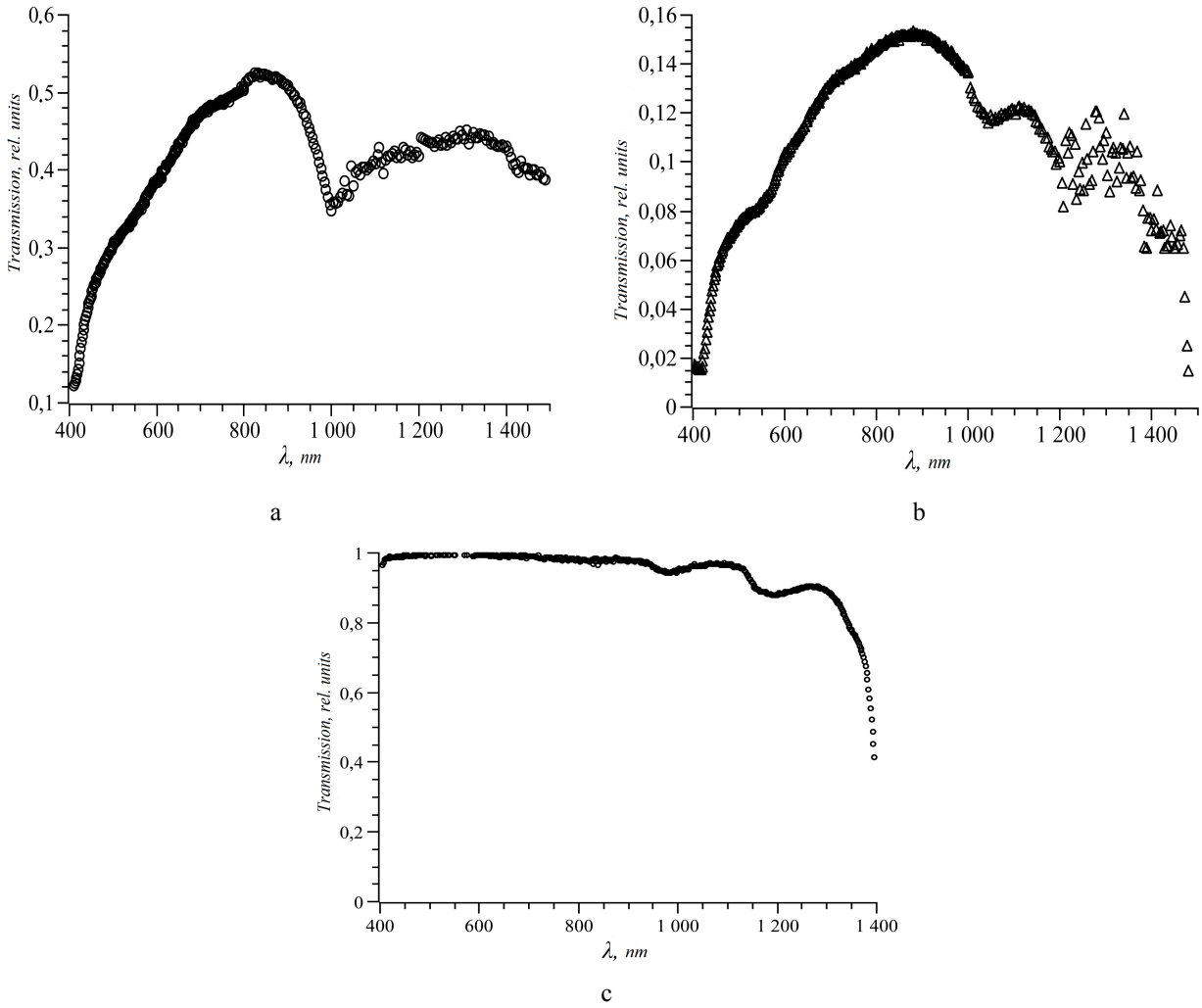

Fig. 1 Spectra of collimated transmission of the cartilage tissue without immersion treatment (a) and subjected to immersion (b); the spectrum of the immersion fluid itself (c).

Table 1 Positions of the absorption peaks for the cartilage tissue in the IR range.

	Wavelength of light λ, nm					
Cartilage tissue after immersion	1049	1207	1239	1307	1361	1488
Cartilage tissue without immersion	1003					1507
Immersion fluid Omnipaque	1050	1200				1450

effect of the immersion fluid on a biotissue leads to the growth of the collagen fibres diameter.

Now let us briefly discuss the analysis of the cartilage tissue images produced by interference of polarised light beams in the biotissue samples. In this case, the sample transmission spectrum is known to depend upon the optical path length difference between the interfering beams and the angle between the optical axis of the sample and those of the polarisers. In our case, the studied samples were strongly nonuniform both in the layer thickness and in the orientation of collagen fibres that determine the orientation of the optical axis of the sample. However, although the variation of the layer thickness is large, as shown by our measurements, its impact on the transmission spectrum (colour) of the sample is small due to the minor value of the cartilage optical anisotropy $\Delta n \approx 0.0004$. Therefore, the different colour of the regions of cartilage tissue is

caused only by the different orientation of collagen fibres (and the resulting difference of the optical axis orientation). This can be easily checked by rotating the microscope object stage through different angles that changes the colour of different regions to the complementary one. In our case, the light regions become dark and vice versa. Thick and thin samples show the same degree of homogeneity in the collagen fibres orientation. This observation means that the samples possess nearly the same number of overlapped layers with different orientation of the collagen fibres. As already mentioned above, the immersion agent does not affect the value of the cartilage tissue optical anisotropy.

4 Diffusion of immersion fluid in the cartilage tissue

As mentioned above, the improvement of the image contrast and the increase of the probing depth can be achieved by applying different immersion fluids that penetrate into the sample [1, 2]. In this connection, it is interesting to study the kinetics of the immersion clearing process in different types of biotissues. Earlier we have studied the influence of the sample geometric parameters on the kinetics of the biotissue immersion clearing process [21]. The diffusion of different substances in a biotissue is often studied using purely optical techniques (see, e.g., [1, 3, 7, 26]), in which the influence of the clearing agent diffusion rate anisotropy (the difference of diffusion rates along the collagen fibres and in the perpendicular direction) and the sample geometry on the diffusion process itself remains unexplored. It is known [1] that, first of all, the geometric parameters of the light-scattering sample strongly affect the light attenuation coefficient, and, therefore, it is necessary to find out, which parameters affect only the diffusion of the immersion fluid and do not affect the optical properties, and which parameters affect both the diffusion kinetics and the attenuation coefficient. In this section of the paper, we report the computer analysis of the kinetics of the immersion fluid diffusion in a biotissue depending on the diffusion rate anisotropy with the fibrillar structure of the studied sample taken into account.

Consider the three-dimensional model of the biotissue immersion clearing, presented in the previous section. To describe the diffusion under the local application of the clearing agent the one-dimensional model has the following drawbacks. 1) In the frameworks of one-dimensional model of the clearing agent diffusion in the biotissue it is impossible to explain the nonmonotonic behavior of transmission as a function of clearing time without attracting other (different from diffusion) possible physical mechanisms that might take place [21]. 2) The determination of the diffusion coefficient of the clearing fluid in the one-dimensional model can yield wrong diffusion rate, since in reality some time is always taken by the diffusion in three directions with different rates, whereas in the one-dimensional model the diffusion is considered to occur only into the depth of the sample. In our case, the model is characterised by the collagen fibre diameter, its length, the mean separation between the fibres and the mean angle of deviation of the fibres from a certain direction, as well as the diffusion rates along the fibres ν_x and in the perpendicular directions ν_y, ν_z. To simplify the analysis, we assumed that the sample is homogeneous in the y and z directions and $\nu_y = \nu_z$.

Fig. 2 illustrates the kinetics of the immersion fluid diffusion in the biotissue under the local application depending on the diffusion rates ν_x and ν_y. The ordinate axis displays the value of the maximal possible concentration of the clearing fluid C_{max} at the fixed depth in the sample. Worth attention is the fact that the diffusion rate increase in the mutually perpendicular planes yields the opposite results. The explanation is that the increase of the diffusion rate ν_x along the fibres leads to the fluid spreading in this direction without penetration deep into the sample. Note that the dependence of C_{max} upon ν_x or ν_y is well described by linear functions, the parameters of which are presented in Fig. 2. The linear character of the dependences $C_{max}(\nu_x)$ and $C_{max}(\nu_y)$ follows from by the fact that the diffusion equation used in our studies is linear and the diffusion coefficients entering this equation are constant. The maximal possible value C_{max} depends on ν_y stronger than on ν_x. The explanation is that with the increase of the diffusion rate across the fibres the immersion fluid more intensely penetrates deep into the sample, while the increase of the diffusion rate along the fibres the immersion fluid spreads over the sample and does not penetrate into it. That is why the increase of the mean rate ν ($\nu = (\nu_x + \nu_y) / 2$) of the diffusion of the immersion fluid in the biotissue can lead to the fall of light transmission instead of its increase, if the increase of the mean rate occurs at the expense of stronger diffusion along the fibres.

As shown by the simulation, the geometric factors (the size of collagen fibres, the separation between them, and the angles of the fibre orientations) weakly affect the kinetics of the immersion fluid diffusion under the local application. The explanation is that the size of the molecules of the diffusing liquid is small compared to the characteristic geometric dimensions of the biotissue structural elements, so that according to the Stokes-Einstein theory [27] the immersion agent diffusion coefficient is determined only by the molecular sizes and the viscosity coefficient of the medium. Hence, the geometric factors of the biotissue strongly affect only the optical parameters of the sample (determining its light attenuation coefficient) and, at the same time, these parameters weakly affect directly the kinetics of the immersion fluid diffusion. Thus, the dependence of the biotissue immersion clearing kinetics on the geometric parameters of the biotissue structure is determined only the dependence of the light attenuation coefficient of the sample upon these factors.

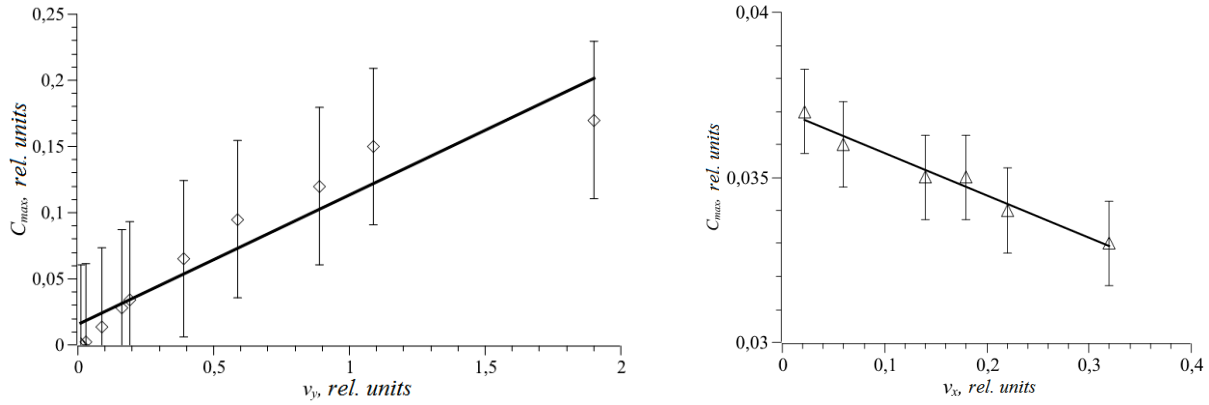

a b

Fig. 2 The concentration of the fluid diffusing into the biotissue versus the diffusion rate (a - in the transverse direction, $C_{max} = b + av_y$; $b = 0.01 \pm 0.008$; $a = 0.1 \pm 0.01$; b - in the longitudinal direction, $C_{max} = b + av_x$; $b = 0.037 \pm 0.0002$; $a = -0.0128 \pm 0.0011$).

5 Conclusion

We presented the experimental and theoretical results of the study of optical and diffusion properties of the cartilage tissue after the immersion clearing procedure and without it. These results can be summarised as follows.

1) The immersion impact on the cartilage tissue leads to its structural changes, increasing the size of the scattering elements, which agrees with the results of Ref. [25].

2) The immersion impact on the cartilage tissue leads to the change of its transmission spectrum in the infrared range. In the visible range, we observed no changes except the increased transmission in the samples subjected to immersion.

3) The immersion impact on the cartilage tissue does not change its refractive index anisotropy. The obtained estimate of the cartilage tissue refractive index anisotropy corresponds to the data of other papers [19, 24].

4) The kinetics of the immersion fluid diffusion in the biotissue strongly depends on the anisotropy of the diffusion rate along the collagen fibres and in the perpendicular direction. The increase of the mean diffusion rate of the immersion fluid in the biotissue under the local application can lead to the fall of light transmission rather than its expected growth.

Disclosures

All authors declare that there is no conflict of interests in this paper.

Acknowledgments

The author is grateful to E.A. Genina, (N.G. Chernyshevky National Research Saratov State University) for valuable recommendations on the use of Omnipaque in optical studies. The author also thanks M.I. Shishkina (N.G. Chernyshevky National Research Saratov State University) for providing the possibility of using the spectral system based on the MDR-41 monochromator.

The work was carried out under the financial support from the Russian Foundation for Basic Research, grant No. 15-29-04810 ofi_m.

In vitro spectroscopic investigation of human cataract lens capsule hydropermeability

Andrey V. Belikov[1], Alexey M. Zagorulko[2], Vyacheslav I. Kochubey[3,4], and Sergey N. Smirnov[1*]

[1] ITMO University, 49 Kronverksky Pr., Saint Petersburg 197101, Russia

[2] St. Petersburg Branch of the S. Fyodorov Eye Microsurgery Federal State Institution, 21 Yaroslav Gashek St., Saint Petersburg 192283, Russia

[3] N.G. Chernyshevsky Saratov State University, 83 Astrakhanskaya St., Saratov 410012, Russia

[4] Tomsk State University, 36 Prosp. Lenina, Tomsk 634050, Russia

***e-mail:** s.n.smirnov@niuitmo.ru

Abstract. The dynamics of collimated transmission of optical radiation in the wavelength range 1100–2000 nm during the *in vitro* dehydration of human cataract lens capsules in air was studied for the first time. For capsules separated from human cataract lenses the average value of the hydropermeability coefficient at dehydration was 0.19±0.10 μm/s. The average characteristic time of cataract lens capsules dehydration was 77±10 s for the samples studied. © 2017 Journal of Biomedical Photonics & Engineering.

Keywords: cataract; eye lens; capsule; capsulorhexis; transmission; laser; water; hydropermeability.

Paper #3214 received 5 Jun 2017; revised manuscript received 14 Sep 2017; accepted for publication 15 Sep 2017; published online 30 Sep 2017. doi: 10.18287/JBPE17.03.030303.

References

1. B. P. Danysh, and M. K. Duncan, "The lens capsule," Experimental Eye Research 88(2), 151–164 (2009).
2. K. Jeon, International review of cell and molecular biology, Volume 296, Academic Press (2012). ISBN: 9780123943071.
3. J. S. Friedenwald, "Permeability of the lens capsule: with special reference to the etiology of senile cataract," Archives of Ophthalmology 3(2), 182–193 (1930).
4. J. S. Friedenwald, "The permeability of the lens capsule to water, dextrose and other sugars," Transactions of the American Ophthalmological Society 28, 195–211 (1930).
5. I. G. Fels, "Permeability of the anterior bovine lens capsule," Experimental Eye Research 10(1), 8–14 (1970).
6. L. Ozaki, "The barrier function of the posterior capsule," American Intra-Ocular Implant Society Journal 10(2), 182–184 (1984)
7. R. F. Fisher, "The water permeability of basement membrane under increasing pressure: evidence for a new theory of permeability," Proceedings of the Royal Society B: Biological Sciences 216(1205), 475–496 (1982).
8. K. Varadaraj, C. Kushmerick, G. J. Baldo, S. Bassnett, A. Shiels, and R. T. Mathias, "The Role of MIP in Lens Fiber Cell Membrane Transport," Journal of Membrane Biology 170(3), 191–203 (1999).
9. K. Varadaraj, S. Kumari, A. Shiels, and R. T. Mathias, "Regulation of Aquaporin Water Permeability in the Lens," Investigative Ophthalmology & Visual Science 46(4), 1393–1402 (2005).
10. K. Varadaraj, S. S. Kumari, and R. T. Mathias, "Functional Expression of Aquaporins in Embryonic, Postnatal, and Adult Mouse Lenses," Developmental Dynamics 236(5), 1319–1328 (2007).
11. C. J. Lee, J. A. Vroom, H. A. Fishman, S. F. Bent, "Determination of human lens capsule permeability and its feasibility as a replacement for Bruch's membrane," Biomaterials 27(8), 1670–1678 (2006).
12. B. P. Danysh, T. P. Patel, K. J. Czymmek, D. A. Edwards, L. Wang, J. Pande, and M. K. Duncan, "Characterizing molecular diffusion in the lens capsule," Matrix Biology 29(3), 228–236 (2010).
13. C. Kastner, M. Lubler, T. Reske, K. Sternberg, R. Guthoff, and K.-P. Schmitz, "Determination of human anterior lens capsule permeability for fluorescent model substances and after-cataract preventive drugs," Biomedical Engineering / Biomedizinische Technik, 57(SI-1 Track-D), 561–563 (2012).

14. K. E. Donaldson, R. Braga-Mele, F. Cabot, R. Davidson, D. K. Dhaliwal, R. Hamilton, M. Jackson, L. Patterson, K. Stonecipher, and S. H. Yoo, "Femtosecond laser-assisted cataract surgery," Journal of Cataract & Refractive Surgery 39(11), 1753–1763 (2013).
15. Z. Z. Nagy, "The role of femtolaser in cataract surgery," European Ophthalmic Review 6(5), 286–289 (2012).
16. V. G. Kopayeva, S. U. Kopayev, A. A. Ginoyan, and V. U. Alborova, "Clinical experience in laser cataract extraction," Bulletin of the Russian Academy of Natural Sciences 1, 77–80 (2012) [In Russian].
17. S. N. Fyodorov, V. G. Kopaeva, Yu. V. Andreev, A. V. Erofeev, A. V. Belikov, E G. Bogdalova, A. V. Skripnik, and O. A. Frolova, "Laser Extraction of Cataract (Experimental studies)," Ophtalmosurgery 3, 3–10 (1998) [in Russian].
18. N. J. Friedman, D. V. Palanker, G. Schuele, D. Andersen, G. Marcellino, B. S. Seibel, J. Batlle, R. Feliz, J. H. Talamo, M. S. Blumenkranz, and W. W. Culbertson, "Femtosecond laser capsulotomy," Journal of Cataract & Refractive Surgery 37(7), 1189–1198 (2011).
19. A. V. Belikov, S. V. Gagarsky, A. B. Gubin, S. Ya. Weiner, A. N. Sergeev, and S. N. Smirnov, "Subjoule diode-pumped ytterbium-erbium glass laser with cavity dumping for cataract extraction," Scientific and Technical Journal of Information Technologies, Mechanics and Optics 15(6), 1021–1029 (2015).
20. A. V. Belikov, S. V. Gagarsky, A. N. Sergeev, and S. N. Smirnov, "In vitro destruction of anterior human lens capsule by submicrosecond pulses of Yb,Er:Glass laser," Proc. SPIE 10336, 103360B (2017).
21. B. S. Ross, and C. A. Puliafito, "Erbium-YAG and Holmium-YAG Laser Ablation of the Lens," Lasers in Surgery and Medicine 15(1), 74–82 (1994).
22. H. Ho, and E. Fischer, "Pilot Study on Erbium Laser Phacoemulsification," Ophthalmology 107(6), 1053–1061 (2000).
23. F. Hausladen, H. Wurm, and K. Stock, "Basic studies on laser-assisted phacoemulsification using diodepumped Er:YAG laser," Proc. SPIE 9693, 96931Y (2016).
24. K. F. Palmer, and D. Williams, "Optical properties of water in the near infrared," Journal of the Optical Society of America 64(8), 1107–1110 (1974).
25. G. M. Hale, and M. R. Querry, "Optical Constants of Water in the 200-nm to 200-μm Wavelength Region," Applied Optics 12(3), 555–563 (1973).
26. A. N. Bashkatov, E. A. Genina, Yu. P. Sinichkin, V. I. Kochubey, N. A. Lakodina, and V. V. Tuchin, "Glucose and Mannitol Diffusion in Human Dura Mater," Biophysical Journal 85(5), 3310–3318 (2003).
27. D. K. Tuchina, R. Shi, A. N. Bashkatov, E. A. Genina, D. Zhu, Q. Luo, and V. V. Tuchin "Ex vivo optical measurements of glucose diffusion kinetics in native and diabetic mouse skin," Journal of Biophotonics 8(4), 332–346 (2015).
28. D. K. Tuchina, A. N. Bashkatov, E. A. Genina, and V. V. Tuchin, "Quantification of glucose and glycerol diffusion in myocardium," Journal Innovative Optical Health Science 8(3), 1541006 (2015).
29. E. A. Genina, A. N. Bashkatov, Yu. P. Sinichkin, I. Yu. Yanina, and V. V. Tuchin, "Optical clearing of biological tissues: Prospects of application in medical diagnostics and phototherapy [Review]," Journal of Biomedical Science & Engineering 1(1), 22–58 (2015).
30. D. K. Tuchina , V. D. Genin, A. N. Bashkatov, E. A. Genina, and V. V. Tuchin, "Optical Clearing of Skin Tissue ex vivo with Polyethylene Glycol," Optics and spectroscopy 120(1), 28–37 (2016).
31. A. N. Bashkatov, "Control of tissue optical properties by means of osmotically active immersion liquids," PhD thesis, Saratov State University, Saratov, Russia (2002) [In Russian].
32. E. A. Genina, A. N. Bashkatov, A. A. Korobko, E. A. Zubkova, V. V. Tuchin, I. Yaroslavsky, and G. B. Altshuler, "Optical clearing of human skin: comparative study of permeability and dehydration of intact and photothermally perforated skin," Journal of Biomedical Optics 13(2), 021102 (2008).
33. A. Kotyk and K. Janáček, Membrane Transport: An Interdisciplinary Approach, Springer US, Plenum Press, New York (1977), ISBN: 978-1-4684-3335-7.

1 Introduction

The lens of the eye does not contain blood vessels; the only filter for the transit of water, nutrients, and products of vital activity is the membrane in which it is housed – the lens capsule. The lens capsule is a thin structureless transparent membrane which completely covers the lens. A part of the capsule that lines the anterior surface of the eye lens is called the anterior lens capsule. From the inside, the anterior capsule is covered with a single-layered epithelium. The devoid of epithelium posterior capsule is almost twice thinner than the anterior. The lens capsule is a matrix of molecules consisting mainly of type IV collagen and laminin networks, which are bound together by nidogen and perlecan [1]. It represents one of the varieties of basement membranes, and is the thickest human basement membrane [2].

Since the viability of the lens is provided by the capsule, interest in the problem of determining the permeability of a given membrane to various substances appeared very long ago. One of the first works on determination of the relative permeability of the lens

capsule to water and various sugars date back to 1930 [3,4].

In [5] the hydrodynamic permeability of the bovine lens capsule to water and the osmotic permeability to glucose were studied. For the investigation of permeability the authors used a device, which represented a U-shaped tube formed by a reservoir ($V = 700$ cm^3) and a thin capillary ($d = 0.1$ mm) between which a sample (capsule) was fixed. The volumetric flow was determined from the magnitude of the height of liquid in the capillary. The need for the fixation of the capsule between two reservoirs (similar constructions were also used in [6–7]), increases the sensitivity of such method to integrity and requires a sufficiently large size of the lens capsule samples. It should be also noted that permeability measurements were carried out under hydrostatic pressure.

In [8–10] the fundamental properties of integral membrane proteins forming pores in membranes of cells –aquaporin's, were studied, their role in the transport of substances through the capsule was investigated. The hydropermeability coefficients of anterior epithelium cells and vesicles of cell membranes of the animal lens fibers were measured.

In [11] the anterior lens capsule of the human eye was examined as a potential replacement for the Bruch membrane for the treatment of age-related macular degeneration. One of the most important properties of the Bruch membrane is the ensuring of a flow of nutrients and products of vital activity between the retinal pigment epithelium and the choriocapillaries. In this connection, the authors measured the lens capsule permeability by studying the diffusion of FITC-dextran molecules (fluorescein isothiocyanate-dextran) with different molecular masses. Diffusion of dextran molecules was performed in a blind-well chamber and the concentration of diffused molecules was measured by recording the fluorescence intensity of the solution.

The studies of the lens capsule permeability, as well as the development of new methods for its measurement, are still relevant. In [12] a method for studying the lens capsule permeability based on the restoration of fluorescence after photobleaching was demonstrated. In [13] the possibility of preventing the occurrence of secondary cataracts by introducing drugs into an artificial intraocular lens was investigated. In this connection, the permeability coefficients of the lens capsule to antiproliferative drugs were measured. The measurements were carried out by the fluorescence detection method, molecular weight cutoff was also measured.

The data on the lens capsule permeability are also of interest for modern ophthalmic surgery, also due to the fact that minimally invasive laser technologies for cataract surgery gain ground. The most commonly used minimally invasive method of cataract surgery is ultrasonic phacoemulsification. Recently, the technology of femtosecond laser-assisted ultrasound phacoemulsification has been actively introduced into surgical practice. In this case femtosecond laser devices are used for opening the anterior lens capsule (capsulorhexis) and pre-softening dense cataract lens [14], but for complete lens fragmentation the additional ultrasonic machine is required. Now, white, brown and black cataracts [15], as well as complications with weak ciliary zonulas [16], are limitations for the application of femtosecond laser-assisted ultrasound phacoemulsification. In ophthalmological clinics in Russia and abroad, along with ultrasonic and femtosecond phacoemulsification, the method of laser cataract extraction (LCE) [17] based on the use of Nd:YAG laser radiation with the wavelength of 1444 nm is widely used. The LCE method is based on the destruction of cataract lenses due to the complex effect of laser radiation and laser-induced acoustic waves. The main advantage of this method is the ability to destruct cataract lenses of any density degree without negative influence on surrounding issues. The lens destruction process is characterized by high productivity - time of complete destruction is of 2–3 minutes [16].

An important stage of minimally invasive cataract surgery, including LEC, is anterior capsulorhexis – opening of the anterior cataract lens capsule. The more precisely capsulorhexis is performed, the more reliable is the fixation of the artificial intraocular lens (IOL), which is installed in the capsular bag at the final stage of the operation as a replacement for the removed cataract lens. Currently, capsulorhexis during LEC is performed either manually, or with the help of complex and expensive femtosecond laser systems. Such laser systems provide a cut of the capsule with the shape of an ideal circle with a given diameter, the edge of the capsule is characterized by greater strength than in the case of manual capsulorhexis [18]. In recent times, the use of a microsecond Yb,Er:Glass laser radiation with a wavelength of 1.54 μm has been discussed [19] for efficient fragmentation of the cataract lens and for performing anterior capsulorhexis [20]. On the other hand, for performing a capsulorhexis it is also possible to use the radiation of lasers on crystalline media activated by erbium ions; the use of Er:YAG laser radiation for lens fragmentation was investigated in [21–23].The radiation of Er:YAG laser with a wavelength of 2.94 μm is very effectively absorbed by water [24,25]; as a result, the penetration depth of this radiation into water-saturated tissues, to which the lens capsule can be attributed, is close to 1 μm. It is obvious that in the process of laser capsulorhexis, during the action of the radiation pulse, the capsule is dehydrated, and in a pause between laser pulses it is saturated with water again. In this regard, in order to select the energy and time parameters of laser radiation for efficient and safe impact on the cataract lens capsule it is important to know how quickly the part of the capsule dehydrated under the action of laser radiation can be saturated with water. The hydropermeability of cataract lens capsules is poorly understood.

Thus, the study of hydropermeability of human cataract lens capsules with the use of effective, non-

contact techniques, including optical techniques, is important and relevant for the development of modern methods of minimally invasive laser cataract surgery. From this point of view, a method for measuring the diffusion properties of biological tissues described in [26–31] is interesting, which is effectively used to study the optical clearing of biological tissues under the action of immersion agents. The method is based on obtaining data on the characteristic times and coefficients of diffusion as well as on the permeability of membranes for osmotically active liquids from data on the dynamics of collimated transmission of optical radiation by samples of biological tissues under the influence of these liquids.

In the present study, the dynamics of collimated transmission of optical radiation in the wavelength range 1100–2000 nm for cataract lens capsules *in vitro* during their dehydration in air was studied for the first time. The analysis of the optical density dynamics made it possible to determine the coefficient of hydropermeability and the characteristic time of dehydration of the human cataract lens capsule.

2 Materials and methods

The samples of human lens capsules were obtained by performing manual capsulorhexis during LEC, after extraction they were stored in saline (0.9% aqueous sodium chloride solution) at a temperature of 4–6 °C. In total, five capsules of medium-density human cataract lenses were examined. To measure the thickness of lens capsules the samples were placed between the coverslips; the measurements were carried out with a micrometer "S_Mike PRO" ("Sylvac", Switzerland).

The determination of the hydropermeability coefficient (dehydration rate) and the characteristic time of dehydration of the cataract lens capsule was carried out on the basis of studying the dynamics of optical signal attenuation associated with the absorption of radiation by the liquid during the dehydration of the capsule in air. This study was carried out in the same way as described in [26–31], where the diffusion of various osmotically active liquids in biological tissues was investigated.

The lens capsule sample was placed onto a glass slide. After that the liquid (saline solution) remaining on the capsule surface was removed mechanically by the lateral surface of injection needle which was moved along the capsule surface. This action was implemented with the minimum possible pressure from the needle side to the capsule sample.

Then a sample of the capsule on the glass slide was placed in the measuring channel of the experimental setup (Fig. 1). The experimental setup included a radiation source (1) – a halogen lamp "HL 2000" ("Ocean Optics", USA), light guides "QP600-2-VIS-NIR" ("Ocean Optics", USA) (2, 5), one of which delivered radiation to the sample (4), the other – collected the radiation transmitted through the sample, a diaphragm (3) with a diameter of 1 mm, a spectrometer (6) "NIR Quest" ("Ocean Optics", USA) and a computer (7).

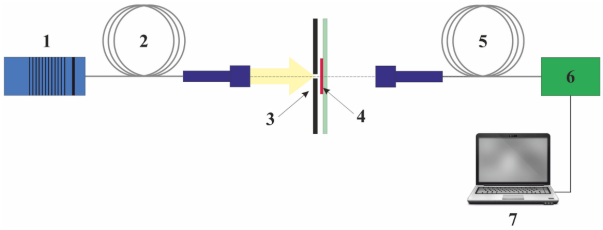

Fig. 1 Scheme of experimental setup for collimated transmission measurement: 1 – halogen lamp "HL 2000" ("Ocean Optics", USA); 2,5 – light guides "QP600-2-VIS-NIR" ("Ocean Optics", USA) with collimators "74-ACR" ("Ocean Optics", USA) at the ends; 3 – diaphragm; 4 – sample on the glass slide; 6 – spectrometer "NIR Quest" ("Ocean Optics", USA), 7 – computer.

In experiment collimated transmission spectra of each sample of lens capsule on a glass slide $T_{glass+sample}(\lambda, t)$ and also spectrum of glass slide $T_{glass}(\lambda)$ were measured in spectral range 1100–2000 nm. The measurements of $T_{glass+sample}(\lambda, t)$ were carried out for the first 3 minutes in 0.5 minute increments, then on 4th, 6th and 10th minute, at room temperature and 20% relative humidity.

The transmission spectra of lens capsule samples $T_{sample}(\lambda, t)$ were obtained by correcting the spectra $T_{glass+sample}(\lambda, t)$ taking into account the absorption of the glass slide and normalization to a transmission value at 1100 nm ($T_{sample}(\lambda = 1100\ \text{nm}, t)$):

$$T_{sample}(\lambda, t) = \frac{T_{glass+sample}(\lambda, t)}{T_{glass}(\lambda) T_{glass+sample}(\lambda = 1100\ \text{nm}, t)}. \quad (1)$$

The wavelength of 1100 nm was chosen as the reference one under the assumption that the scattering coefficients for a transparent capsule are small and close to each other for the investigated spectral range, and the absorption of water at a given wavelength is negligible (Fig. 2).

A baseline drift of the measuring device causes the need for such a normalization during the experiment. The baseline drift may be connected with the time variation of the refractive index of the sample (due to dehydration) when the glass slide with the sample is not perpendicular to the light beam. The baseline drift may be also associated with incompletely aligned sphericity of the sample when placed onto the glass slide, which leads to shift of the beam relative to the optical axis. The normalized collimated transmission spectra were averaged over five samples, after that the spectral dependences of the average optical density were obtained from the average transmission spectra:

$$D(\lambda,t)=\lg\left(\frac{1}{T_{sample}(\lambda,t)}\right). \qquad (2)$$

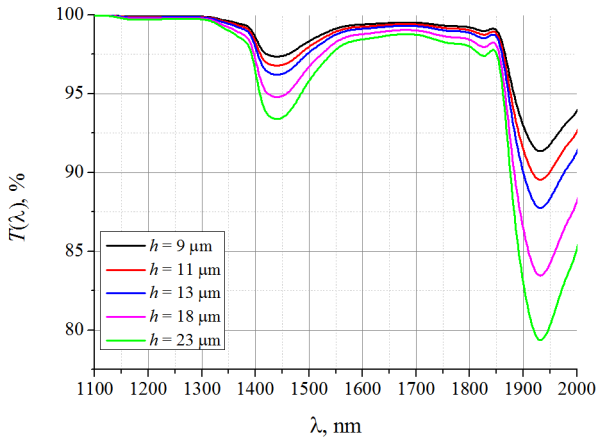

Fig. 2 Transmission spectra $T(\lambda)$ of water layers of thickness h equal to thickness of investigated lens capsule samples.

The time variation in the optical density of lens capsules at the wavelength of 1950 nm, which align with the local absorption peak of water contained in the lens capsule, is associated with the dehydration of the capsule. Dehydration, in turn, is associated with the diffusion of water from the sample into the external volume. In this connection, the dynamics of the dehydration degree change can be described using the equation for diffusion through the permeable membrane. For estimation of dehydration degree under the action of air, the following equation can be used [30]:

$$\frac{C(t)}{C_0}=\frac{M(t)-M_{res}}{M(t=0)-M_{res}}=\exp\left(-\frac{t}{\tau_D}\right), \qquad (3)$$

where M is the mass of the biotissue sample, M_{res} is the residual mass of the sample (i.e., completely dehydrated), C is the concentration of the diffusing substance, C_0 is the concentration of the substance in the closed volume at the initial time, τ_D is the time constant characterizing the dehydration rate and t is the dehydration time.

The parameter M_{res} includes the mass of collagen, elastin and other components of the tissue after complete dehydration, bound water and possible residual free water. The difference between the initial and residual mass of the sample (M (t = 0) – M_{res}) indicates the amount of water which left the tissue due to dehydration.

Eq. (3) is similar in shape to the diffusion equation, which describes the flow of substance from a small volume with a nonzero concentration to a tank of zero concentration [31]:

$$C(t)=C_0\exp\left(-\frac{PS}{V}t\right), \qquad (4)$$

where C_0 is the concentration of substance in a closed volume at the initial time, P is the permeability coefficient, S is the area of the membrane and V is the closed volume.

The permeability coefficient P of membrane in the case of one-sided diffusion is related to the characteristic diffusion time τ_D of water in the capsule by the expression:

$$P=\frac{h}{\tau_D}, \qquad (5)$$

where h is the membrane thickness.

Since the optical density of the lens capsule at the wavelength of 1950 nm is directly proportional to the concentration of water contained in it, taking the sample thickness unchanged during the measurements, the dynamics of the sample optical density change $D(t)$ during its dehydration by analogy with equation (3) can be described by the following expression

$$D(t)=\left(D(t=0)-D_{res}\right)\exp\left(-\frac{t}{\tau_D}\right)+D_{res}, \qquad (6)$$

where t is the dehydration time, τ_D is the time constant characterizing the dehydration rate, D_{res} is the residual optical density associated with the absorption of radiation by a dry matter and possible residual water.

Thus, the average for the samples studied characteristic dehydration time of human cataract lens capsules (the characteristic water diffusion time τ_D in the capsule) can be obtained by approximating the experimentally obtained points of the time dependence of the optical density of the samples at the wavelength of 1950 nm.

In our study, the approximation of the experimental data was carried out by using non-linear fitting with final value fixation in the package "OriginPro 8.5.1" (OriginLab Corp., USA). The following standard exponential function was used

$$y(x)=A\exp(Bx)+C. \qquad (7)$$

The program generated the values of approximation coefficients and corresponding values of standard deviation.

3 Results and discussion

Averaged over all samples spectra of optical density at different times are shown in Fig. 3a. Figure 3b shows the experimentally obtained values of optical density of the lens capsules at the wavelength of 1950 nm at different times and the results of the approximation of

these values by the function (7). It is seen that in the first 3 minutes the optical density at the wavelength of 1950 nm drops fast, then a segment of slower bleaching is observed.

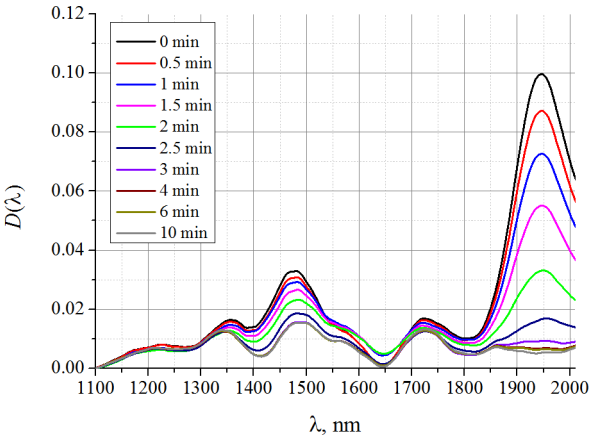

a

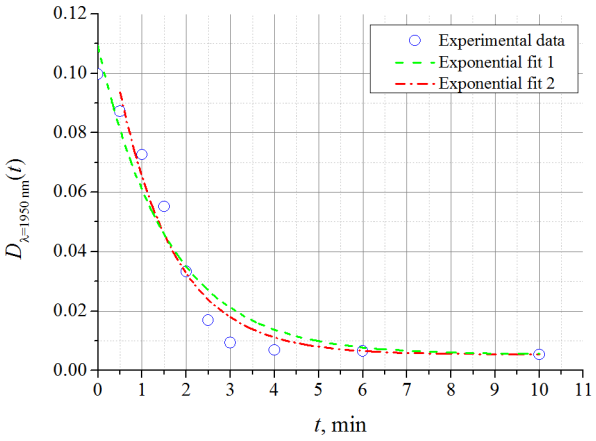

b

Fig. 3 Lens capsule optical density spectra D (λ) obtained according Eq. (2) in different time points **(**a**)**; dependence of lens capsule optical density $D_{\lambda=1950\ \mathrm{nm}}(t)$ at the wavelength of 1950 nm on dehydration time **(**b**)**.

The accuracy of the result can be affected by the fact that the thickness of the sample as decreases during the dehydration (drying). The point D (t = 0) can introduce an error in the result of approximation due to a inconstancy of the time interval between the moment of setting the glass slide with the sample into the measuring channel and the moment of the beginning of transmission spectrum measurement. In this connection, in Fig. 3b two versions of the experimental points approximation are presented, taking into account the point D (t = 0) ("Exponential fit 1") and with its exception ("Exponential fit 2").

As a result of the "Exponential fit 2" approximation the mean over samples studied value of characteristic time of dehydration (diffusion of water from the sample) of the anterior cataract lens capsule was obtained: $\tau_D = 77 \pm 10$ s. By using "Exponential fit 1", this value was 95 ± 12 s. In our opinion, the result obtained with "Exponential fit 2" with the exception of the point D (t = 0) is more adequate.

The indicated error in the result is an error of approximation. At an average of five capsule thicknesses of $h = 14.8 \pm 5.7$ μm and a dehydration time of $\tau_D = 77 \pm 10$ s, the average value of the permeability coefficient P calculated according to Eq. (5) is $P = 0.19 \pm 0.10$ μm/s.

In our experiment, the capsules were not cleared from the anterior lens epithelial cells, so the latter had an effect on the permeability. It should be noted that the obtained value of the permeability coefficient of cataract lens capsule is two orders of magnitude less than the values of permeability coefficients of anterior lens epithelial cells, presented in [8, 10]. In [3] a significant decrease in the permeability of the lens capsule in the case of cataract was noted, so the observed difference in results can be explained by the fact that in our case capsules separated from the human cataract lenses were examined. It is also worth noting the fact that in our case the dehydration of the capsule took place in the air, while in [8,10] the shrinking of cells caused by the change of saline osmolality from 240 mM to 480 mM was analyzed.

A comparison of the obtained results with the data on the lens capsule permeability coefficients obtained in [3-7] presents difficulties, because in these studies the measurements were carried out in the presence of hydrostatic pressure.

If we assume that the width of the dehydrated tissue zone near the boundary of laser-produced microperforation in capsule is comparable to the penetration depth of laser radiation, then for lasers on crystalline media activated by erbium ions (for example, Er:YAG laser), it amounts to about 1 μm. Taking into account the hydropermeability coefficient measured in this paper, this zone will restore the initial water content, and hence the initial absorption coefficient, only on average 5 s after laser exposure. Thus, for effective capsulorhexis by means of erbium laser radiation this feature should be taken into account when choosing a technology for scanning a laser beam over the surface of the capsule.

4 Conclusion

The paper describes a method for measuring the hydropermeability of the lens capsule and the characteristic time of its dehydration in air using optical spectroscopy. For capsules separated from the cataract lenses of the human eye the average over studied samples value of hydropermeability coefficient was 0.19 ± 0.10 μm/s. The average characteristic time of dehydration was 77 ± 10 s. The method can be used for express studies of lens capsule samples in order to obtain information about their physical condition. The results obtained with the help of this method are useful when tuning laser sources for capsulorhexis in laboratory for choosing optimal radiation parameters. The data on lens capsule hydropermeability indicate a possibility of cataract development; therefore, the

method can also be used for studies of the influence of various drugs on eye lens. The determination of the possibility of using such method in clinical practice requires additional research and the development of special equipment.

Disclosures

The authors declare that there are no conflicts of interest related to this article.

Acknowledgments

The work was carried out under the partial financial support from the Russian Foundation for Basic Research, grant No. 16-32-50164.

Potentialities of Digital Capillaroscopy in the Diagnostics of Oedema Syndrome

Yury I. Gurfinkel[1]*, and Maria L. Sasonko[2]

[1] Laboratory of blood microcirculation, Medical Research and Educational Center, Lomonosov Moscow State University, Moscow, Russia

[2] Research Clinical Centre, JSC Russian Railways, Moscow, Russia

*** e-mail:** yugurf@yandex.ru

Abstract. The paper is devoted to the study of digital capillaroscopy potentialities in the assessment of oedema syndrome by the example of a group of patients with diseases of cardiovascular system (CVS). 75 patients were examined, 47 of them with CVS diseases and 28 healthy volunteers. Alongside with the standard examination customary for this pathology, the capillaroscopy of hand finger nail bed was carried out in all patients. The study has revealed considerable dilation of transitional segments of capillaries, increase of the capillary bed remodelling coefficient and the linear dimension of perivascular zone in patients with clinically expressed oedema syndrome. In the group of patients with CVS diseases without clinically expressed oedema, we revealed the statistically significant increase of perivascular zones and remodelling coefficient of capillary bed. The digital optical capillaroscopy can be applied in the clinical practice for early diagnostics of the hidden oedema syndrome and as a quantitative method of diagnostics for clinically expressed oedema and assessment of drug therapy efficiency.

Keywords: digital capillaroscopy; oedema syndrome; remodelling coefficient; perivascular zone.

Paper #3218 received 13 Jan 2017; revised manuscript received 13 Mar 2017; accepted for publication 15 Jun 2017; published online 7 Jul 2017. doi: 10.18287/JBPE17.03.030401. [Special Issue. Years in Biophotonics: 70th Anniversary of Prof. A.V. Priezzhev].

References

1. G. Yu. Suvorova, and A. I. Martynov, Oedema syndrome: clinical presentation, differential diagnostics, treatment, GEOTARMedia, Moscow, Russia (2009) [in Russian].
2. V. Yu. Mareyev, M. O. Danielyan, Yu. N. Belenkov, et al, "Epidemiologic examination of patients with CHI in real practice (by medical aid appealability)," EPOKhA-O-KhSN study, Serdechnaya nedostatochnost' 4(3), 116-120 (2003) [in Russian].
3. P. Ponikowski et al., "ESC Guidelines for the diagnosis and treatment of acute and chronic heart failure," European Journal of Heart Failure 18, 891-975 (2016).
4. A. J. Houben, J. H. Beljaars, L. Hofstra, A. A. Kroon, and P. W. de Leeuw, "Microvascular Abnormalities in Chronic Heart Failure: A Cross-Sectional Analysis," Microcirculation 10(6), 471-478 (2003).
5. Yu. I. Gurfinkel', O. V. Makeyeva, and V. A. Ostrozhinskii, "Peculiarities of microcirculation, endothelial function, and the pulse wave propagation velocity in patients with initial stages of arterial hypertension," Funktsional'naya diagnostika 2, 18-25 (2010) [in Russian].
6. Yu. I. Gurfinkel', O. Yu. At'kov, M. L. Sasonko, and R. M. Sarimov, "New approach to the integral assessment of the cardiovascular system condition in patients with arterial hypertension," Rossiyskii kardiologicheskii zhurnal 105(1), 101-106 (2014).

1 Introduction

The oedema syndrome is a combination of signs characterising the retention of liquid in the organism with its predominant accumulation in tissues. It is most clearly manifested by peripheral oedema [1]. The oedema syndrome is often met in clinical practice, particularly, in patients of elder age groups. Frequently the patient seeks medical attention with the main complaint of oedema appearance, and exactly at this moment, it is important to estimate correctly the character and the degree of expression of the oedema syndrome.

The most frequent cause of oedema syndrome development in elderly persons is the heart failure (HF) as an outcome of different diseases of cardiovascular system (CVS), such as the arterial hypertension, coronary heart disease, etc. In European countries, the HF occurrence amounts to 2-4% of the population. In Russia, the HF occurrence amounts to 7% of the population [2]. The absence of specific symptoms and objective signs of the disease may complicate the diagnostics of CHI. However, according to the documents of the European Society of Cardiology, insignificant or moderate manifestations of HF are fraught with serious risk of hospitalisation and death, which makes it necessary to seek for new diagnostic possibilities of objective assessment of the patient's condition [3].

The cardiovascular diseases (CVDs) are known to affect the microcirculatory bed essentially. As shown by the study of the capillary network density, the diameter and morphology of microvessels of bulbar conjunctiva and finger nail bed in patients with HF, carried out in the Netherlands, the significant impairment of capillary bed parameters accompanies the HF, its expression being the greater the more severe the illness is [4]. At the same time, it is worth noting that the procedure of oedema syndrome diagnostics by general practitioners has not been essentially improved during long time and in most cases is descriptive rather than quantitative.

The aim of the study is to analyse the potentialities of the digital optical capillaroscopy in the diagnostics of oedema syndrome in patients with the diseases of cardiovascular system.

2 Patients and methods

The study was performed in 75 persons, including 47 patients and 28 healthy volunteers. The examined patients suffered from arterial hypertension, coronary heart disease, including patients with myocardial infarction in history. The exclusion criteria were the presence of chronical varix dilatation, oncologic diseases, system diseases of connective tissue, hepatic and renal insufficiency, pregnancy and lactation.

The first group consisted of 19 patients (mean age 54.3 ± 10.5 years old) having no clinically expressed oedema syndrome (Table 1). In the patients of this group, we observed insignificant limitation of physical activity, transitory (evening) pastosity of ankles, shins, and feet. The second group included 28 patients (mean age 57.7 ± 9.4 years old), in which even minor physical loads led to the appearance of palpitation and dyspnoea. Besides that, they had expressed oedema of ankles, shins, and feet. All patients received combined drug treatment daily (Table 2).

Investigation of blood capillaries and surrounding tissues parameters of the finger nail bed was implemented using the digital capillaroscope ("Kapillaroskan-1", Russia), equipped with high-speed video camera that provided video file recording with the rate of 200 frames per second. The day before the examination, the patients and volunteers did not smoke and did not use caffeine-containing drinks. The examination was carried out in the sitting position after 15-20 minutes of rest under the conditions of constant temperature in the room (22-24°C), before taking the morning dose of drugs. The capillary blood flow was studied in the eponychium of the fourth or third finger of the left hand. The finger under study was fixed in a special holder with soft pressing of the middle phalange dorsal surface, providing full immobilisation during the examination. The temperature of the nail phalange near the eponychium was measured using the contactless thermometer Ri-thermo N (Riester, USA). With the magnification of 400×, at least 6-10 video fragments were recorded for further quantitative analysis.

The processing of raw information was implemented using the software that allowed the viewing of the recorded video fragments, the measurement of capillary diameters in the arterial, transitional, and venous segments. The linear size of the perivascular zone was defined as the separation between the most distant point of the perivascular zone and the closest point of the capillary transitional segment.

Table 1 Clinical presentations in the groups of patients with diseases of cardiovascular system.

Group of patients	Physical activity and clinical presentations
Group 1 (n=19)	Insignificant limitation of physical activity. The physical load can cause fatigability, palpitation, dyspnoea. Ankle and shin transient pastosity. No oedema in feet, ankles and shins.
Group 2 (n=28)	Limitation of physical activity. Insignificant loads lead to palpitation and dyspnoea. Expressed oedema of feet, ankles and shins

Table 2 Clinical characterisation of the groups under study.

Parameter	**Control group (n = 28)**	**Patients with cardiovascular diseases (n = 47)**
Age, years	56.4±7.5	57.0±9.1
Sex, m/f, %	74/26	79/21
Body mass index, kg/m^2	28.4±5.62	29.2±7.6
Smoking, *%*	41	34
Ejection fraction, *%*	64.8±5.2	53.9±12.1*
Arterial hypertension, %	-	68
Type-2 diabetes, *%*	-	25
Postinfarction cardiosclerosis, *%*	-	41
Drug therapy, *%*		
β-blocking agents	-	58.9
ACE inhibitors / Sartans	-	88.6
Calcium antagonists	-	25.9
Diuretics	-	57.9
Statines	-	64.4
Nitrates	-	15.8

Note: The asterisk marks the parameter, for which the difference between the groups is statistically significant.

To estimate the degree of capillary constriction, we used the coefficient of capillary bed remodelling (CCBR), introduced by us earlier as a ratio of the mean capillary diameter in the venous segments and the mean capillary diameter in the arterial segments [5, 6].

2.1 Statistics

The statistical differences between the groups were determined using the Student criterion. The normality of the parameters distribution was assessed using the Kolmogorov-Smirnov criterion. The plurality of comparison was taken into account by means of the false discovery rate method. The results are presented in the tables as M ± m, where M is the mean value of the parameter and m is the standard deviation. The statistical analysis was carried out using the standard statistical software package IBM SPSS Statistic 20.

3 Results

The basic characterisation of the groups is presented in Table 2. The studied groups are comparable in age, sex and smoking status. The patients had significantly higher body mass index and essentially lower index of global left ventricle myocardial contractility then the healthy volunteers.

The results of comparison of the measured parameters in the group of healthy volunteers and the subgroups of patients with CHI are presented in Table 3.

In comparison with the healthy volunteers, in the patients of the first group we revealed decreased level of systolic and diastolic arterial pressure and pulse rate. The presence of patients with type-2 diabetes in this group explains the increased blood glucose level. The ejection fraction of the left ventricle stayed within the interval of normal values, but was significantly lower than in the control group. The analysis of the microcirculation parameters revealed the statistically significant increase of perivascular zone size and CCBR.

In the patients of the second group the levels of arterial pressure and pulse rate did not significantly differ from those of healthy volunteers. We noticed the decrease of the global contractility of myocardium. The changes of microcirculation parameters in this group were most strongly expressed. The linear size of the perivascular zone was significantly increased, the mean value of the transitional segment and CCBR were significantly higher than in the group of healthy volunteers.

Table 3 Distribution of the measured parameters in the groups under study.

Parameter	Control group (n=28)	Patients with diseases of cardiovascular system (n = 47)			
		Group 1 (n=19)	p-level	Group 2 (n = 28)	p-level
SAP, *мм рт.ст.*	127.3±6.3	**121.4±14.3**	**0.032**	128.7±15.4	0.557
DAP, *мм рт.ст.*	78.6±7.0	**76.1±10.9**	**0.028**	80.8±9.2	0.342
Pulse, min^{-1}	71.9±12.1	**67.7±11.1**	**0.039**	72.8±11.6	0.715
PZ, *μm*	101.3±14.6	**109.4±10.7**	**0.004**	**151.1±16.5**	**0.000**
AS, *μm*	9.4±2.2	9.8±2.4	0.465	9.6±4.5	0.607
TS, *μm*	13.5±3.1	15.2±4.4	0.117	**17.5±4.4**	**0.001**
VS, *μm*	12.8±3.2	13.9±3.2	0.119	15.0±3.9	0.677
CCBR	1.33±0.1	**1.44±0.2**	**0.035**	**1.51±0.30**	**0.031**
EF, *%*	64.8±5.2	**56.4±8.9**	**0.001**	40.2±10.1	**0.000**
Creatinine, *μmol/l*	95.1±16	96.2±15	0.645	**124.5±36**	**0.000**
Urea, *mmol/l*	5.9±0.9	7.8±1.1	0.446	**7.0±2.2**	**0.023**
Glucose, *mmol/l*	5.5±0.5	**6.2±0.9**	**0.015**	5.9±0.6	0.332

Note: SAP - systolic arterial pressure; DAP - diastolic arterial pressure; EF-ejection fraction; PZ - perivascular zone; AS - arterial segment; TS - transitional segment; VS - venous segment. The comparison was carried out between the groups of patients with the diseases of cardiovascular system and healthy volunteers. In boldface the parameters with statistically significant differences between the groups are given.

4 Discussion of results

Until recently, the capillaroscopy of the hand finger nail bed was not used to assess the condition of cardiovascular system in patients with oedema syndrome. The present paper demonstrates the presence of essential changes of microcirculation parameters in the patients with clinically expressed oedema. Considerable increase of the linear size of perivascular zone in the patients with oedema syndrome as compared to the healthy volunteers was found. The increase of the perivascular zone is probably due to the increase of pressure in the transitional segments of the capillaries, leading to the increase of the capillary diameter in these sections and the activation of liquid release into the perivascular space. The increase of the capillary transitional segment size in our study appeared to be characteristic for the patients with more expressed oedema syndrome (the second group). In the patients of the first group (without clinically expressed oedema) the size of perivascular zone also demonstrated statistically significant difference from that in healthy volunteers, i.e., the increase of the linear size of perivascular zones is not a significant quantitative sign of the oedema syndrome only, but also can be revealed in the patients with hidden oedema.

Against the background of drug therapy, the clinical signs of oedema syndrome can essentially regress, which can be quantitatively assessed by capillaroscopy. Fig. 1 presents the capillarogram of the patient U., admitted to the hospital with expressed oedema syndrome.

The capillaroscopy of hand finger nail bed was executed at the third day of the diuretic therapy, against the background of which the clinical compensation of the oedema syndrome was achieved. The perivascular zone size amounted to 118 μm (the solid line, **A**). Simultaneously the second contour of the perivascular zone (dashed line, **B**) at the distance of 174 μm was determined, corresponding to the initial level of the oedema syndrome. Thus, the linear size of the perivascular zone reflects well the condition of the pericapillary oedema. The obtained data can be used for personal quantitative assessment of the oedema syndrome expression, including that against the background of treatment.

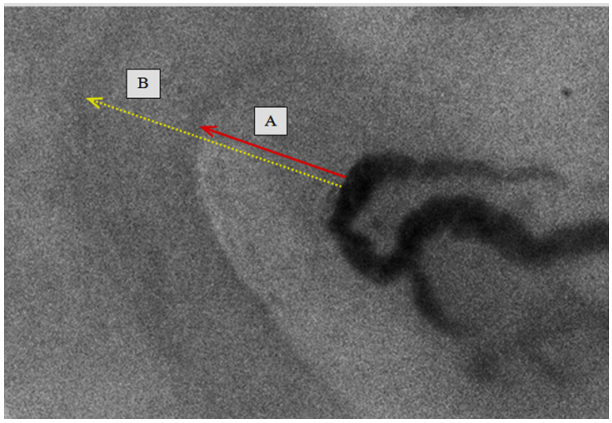

Fig. 1 Dynamics of linear dimension of perivascular zone (PZ) against the background of diuretic therapy. **A** – against the background of treatment (PZ = 118 μm). **B** – before the beginning of treatment (PZ = 174 μm).

The increase of the perivascular zone can be revealed not only in the presence of cardiovascular pathology. Clinical observation revealed the oedema of the perivascular tissues of the finger nail bed in the case of receiving a large portion of liquid, salt, alcohol, of chronical venous insufficiency, systemic diseases of the connective tissue. However, the increase of perivascular zone revealed by capillaroscopy is a reason for thorough diagnostic examination of the patients aimed at determining the aetiology and pathogenesis of the oedema syndrome.

5 Conclusions

The study has shown the significance of the digital capillaroscopy of hand finger nail bed in the diagnostics of the oedema syndrome. In the patients with oedema syndrome significant deviations of the capillary parameters and surrounding tissues were revealed in comparison with the healthy volunteers.

The increase of the mean diameter of transitional segments of capillaries, the remodelling coefficient and the linear size of perivascular zone in the capillaroscopy of hand finger nail bed are significant markers of the oedema syndrome.

The digital optical capillaroscopy can be applied in the clinical practice for early diagnostics of the hidden oedema syndrome, and as a quantitative diagnostic method for clinically expressed oedema and the efficiency assessment of drug therapy.

Disclosures

All authors declare that there is no conflict of interests in this paper.

Acknowledgment

The study was supported by the Russian Scientific Foundation, grant No. 14-15-00602.

Hemorheological properties in patients with type-1 and type-2 diabetes mellitus

Irina A. Sokolova[1], Aleksandrina V. Kachalova[1,2], Anastasiya A. Fabrichnova[2], Yulia A. Kovaleva[3], Aleksandr A. Shahnazarov[1], and Vladimir B. Koshelev[2*]

[1] Laboratory of Biomechanics, Institute of Mechanics, M.V. Lomonosov Moscow State University, Michurinsky pr., 1, Moscow 119192, Russia

[2] Faculty of Fundamental Medicine, M.V. Lomonosov Moscow State University, Lomonosovsky pr., 27-1, Moscow 119991, Russia

[3] Department of Therapeutic Endocrinology, M.F. Vladimirsky Moscow Regional Research and Clinical Institute, Shepkina str., 61/2, Moscow129110, Russia

*** e-mail:** vkoshelev@fbm.msu.ru

Abstract. The hemorheologic disorders, which are potentially deleterious in a wide range of pathologies, were studied in patients with type-1 and type-2 diabetes mellitus. The significant determinants of blood viscosity, red blood cells (RBC) deformability and RBC reversible aggregation were assessed by ektacytometry and by laser backscattering technique, respectively. For both types of the disease, we observed acceleration of the first phase of RBC aggregation that contrasted with its deceleration at the second phase. The hydrodynamic stability of the aggregates, especially the smallest ones, exceeded the normal values in both cases. The influence of GP IIb/IIIa receptor inhibitor, monafram on RBC aggregation and disaggregation was the same in the cases of patients and normal subjects. The maximal shear induced RBC stretching exceeded the normal one in patients of both groups. The data reveal not only pathological but also compensatory character of hemorheological alterations in patients with type-1 and type-2 diabetes mellitus.

Keywords: diabetes mellitus; RBC aggregation; RBC deformability; monafram.

Paper #3219 received 16 Jan 2017; revised manuscript received 15 Feb 2017; accepted for publication 15 Jun 2017; published online 13 Jul 2017. doi: 10.18287/JBPE17.03.030402. [Special Issue. Years in Biophotonics: 70th Anniversary of Prof. A.V. Priezzhev].

References

1. H. J. Meiselman, "Red blood cell aggregation: 45 years being curious," Biorheology 46(1), 1–19 (2009).
2. J. Radosinska, and N. Vrbjar, "The role of red blood cell deformability and Na,K-ATPase function in selected risk factors of cardiovascular diseases in humans: focus on hypertension, diabetes mellitus and hypercholesterolemia," Physiol. Res. 65(Suppl. 1), S43-S54 (2016).
3. S. Mendis, S. Davis, and B. Norrving, "Organizational Update: The World Health Organization Global Status Report on Noncommunicable Diseases 2014; One More Landmark Step in the Combat Against Stroke and Vascular Disease," Stroke 46, e121-e122 (2015).
4. P. Vague, and I. Juhan, "Red cell deformability, platelet aggregation, and insulin action," Diabetes 32(Suppl. 2), 88-91 (1983).
5. C. Lacombe, C. Bucherer, and J. C. Lelievre, "Hemorheological improvement after Daflon 500 mg treatment in diabetes," Int. Angiol. 7(Suppl. 2), 21-24 (1988).
6. M. Cho, S. Shin, H. M. Kwon, H. Chung, and B. K. Lee, "Effect of clinical and RBC hemorheological parameters on myocardial perfusion in patients with type 2 diabetes mellitus," Biorheology 51(2-3), 215-226 (2014).
7. N. Pargalava, M. Mantskava, and G. Mchedlishvili, "Regional and systemic hemorheological disorders during feet diabetic gangrene," Clin. Hemorheol. Microcirc. 30(3-4), 457-459 (2004).

8. G. Cicco, and S. Cicco, "Hemorheology and microcirculation in some pathologies of internal medicine," Minerva Med. 98(6), 625-631 (2007) [in Italian].
9. S. Chien, and K.-M. Jan, "Ultrastructure basis of the mechanism of rouleaux formation," Microvascular Research 5, 155-166 (1973).
10. D. Lominadze, and W. Dean, "Involvement of fibrinogen specific binding in erythrocyte aggregation," FEBS Lett. 513(1-3), 41–44 (2002).
11. I. A. Sokolova, A. V. Muravyov, M. D. Khokhlova, S. Y. Rikova, E. V. Lyubin, M. A. Gafarova, M. N. Skryabina, A. A. Fedyanin, D. V. Kryukova, and A. A. Shahnazarov, "An effect of glycoprotein IIb/IIIa inhibitors on the kinetics of red blood cells aggregation," Clin. Hemorheol. Microcirc. 57(3), 291-302 (2014).
12. E. Straface, R. Rivabene, R. Masella, M. Santulli, R. Paganelli, and W. Malorni, "Structural changes of the erythrocyte as a marker of non-insulin-dependent diabetes: protective effects of N-acetylcysteine," Biochem. Biophys. Res. Commun 290(5), 1393-1398 (2002).
13. M. Donner, M. Siadat, and J. F. Stoltz, "Erythrocyte aggregation: approach by light scattering determination," Biorheology 25(1-2), 367-375 (1988).
14. M. Bessis, and N. Mohandas, "A diffractometric method for the measurement of cellular deformability," Blood Cells 8(3), 307-313 (1975).
15. T. V. Korotaeva, N. N. Firsov, A. Bjelle, and M. A. Vishlova, "Erythrocytes aggregation in healthy donors at native and standard hematocrit: the influence of sex, age, immunoglobulins and fibrinogen concentrations. Standardization of parameters," Clin. Hemorheol. Microcirc. 36(4), 335-343 (2007).
16. N. N. Firsov, N. V. Klimova, A. V. Priezzhev, and A. Yu. Tyurina, "Fundamental laws of the deformational behaviour of erythrocytes in shear flow," Journal of Engineering Physics and Thermophysics 79(1), 118-124 (2006) [in Russian].
17. O. V. Filatova, A. A. Sidorenko, and S. A. Agarkova, "Effects of age and sex on rheological properties of blood," Human Physiology 41(4), 437-443 (2015) [in Russian].
18. M. Mantskava, N. Momtselidze, N. Pargalava, and G. Mchedlishvili, "Hemorheological disorders in patients with type 1 or 2 diabetes mellitus and foot gangrene," Clin. Hemorheol. Microcirc. 35(1-2), 307-310 (2006).
19. I. Sokolova, M. Gafarova, M. Khokhlova, A. Muravyev, E. Lyubin, M. Skryabina, A. Fedyanin, T. Krasnova, and A. Shahnazarov, "Glycoprotein IIB-IIIA inhibitor, monafram decelerate the early phase of red blood cells aggregation," Journal of Cellular Biotechnology 2(1), 15-22 (2016).
20. W. Subasinghe, and D. M. Spence, "Simultaneous determination of cell aging and ATP release from erythrocytes and its implications in type 2 diabetes," Anal. Chim. Acta. 618(2), 227-233 (2008).

1 Introduction

The abnormalities of biophysical properties of blood are often related to enhanced RBC rigidity, which results in microcirculatory disturbances and aggravation effects in different diseases [1, 2]. One of these diseases is the diabetes mellitus (DM) that now has the character of a non-infection epidemy because of its prevalence [3]. DM is characterised by the absolute or relative deficiency of insulin, leading to hyperglycaemia, and long ago it was revealed that DM can accompanied by the decreased RBC deformability and enhanced RBC aggregation [4, 5]. These hemorheological disturbances can give rise to ischemic-related tissue damage and stimulate the development of different complications [6]. At the same time, the role of hemorheological pathology in DM is not undisputable: some researchers noted its presence mainly in local regions or did not observe it at all [7, 8]. The mechanisms of enhanced RBC aggregation are also still unclear. Whatever the explanation of this phenomenon is (the non-specific interaction of biopolymer molecules, mainly fibrinogen, with cell membranes and, hence, the RBC linking by polymer "bridges" [9], or the relative reduction of the macromolecules concentration near the cells surface, giving rise to attractive osmotic forces [1]), the mechanisms of RBC aggregation are mainly considered to be non-specific. Nevertheless, the specific fibrinogen receptors were revealed at RBC membrane [10], and it is possible that, in pathologic cases, this specific fibrinogen–RBC interaction can enhance the stability of RBC aggregates [11]. In patients with DM, the RBCs were shown to possess some specific features [12], but their possible receptor interaction with fibrinogen (which, in contrast to non-specific coupling, could be subject to pharmacological intervention) remains practically unstudied.

The objective of this study was to investigate RBC deformability and aggregation in patients with diabetes mellitus and, in addition, we aimed to evaluate a possibility of specific fibrinogen binding by RBC membrane as one of the factors which contribute to RBC aggregation in this disease.

2 Materials and methods

2.1 Subjects

Blood samples were collected from patients with type-1 or type-2 diabetes mellitus (DM1 and DM2, respectively) and from healthy volunteers of comparable sex and age. The patients were hospitalized in the Department of Therapeutic Endocrinology of the M.F

Vladimirsky Moscow Regional Research and Clinical Institute (MONIKI), where they passed the standard clinical and laboratory examination. The study was carried out in accordance with the protocols, approved by the Ethics Committee of the MONIKI and FFM MSU, after the receipt of informed consent from all the donors.

The blood samples were withdrawn from the elbow median vein (v. mediana cubiti) and stabilized with ethylene diamine tetraacetate (EDTA, 2 mg/ml). They were tested within 2 hours after the sampling.

2.2 Hemorheological analysis

The kinetics of RBC aggregation was studied using the light backscattering method [13], and the RBC deformability was tested by means of the ectacytometry method [14] using the coaxial cylindrical aggregometer-deformometer LADE (the rheological gap 0.9 mm, λ=650 nm, the laser radiation power 1 mW, ReoMedLab, Ltd., Russia) at the temperature 25°C. The cells reversible aggregation was studied under the hematocrit (Hct) ~0.40 that was standardized by correcting the Hct of the whole blood. In the course of the experiment after a short period of high-velocity flow, the flow was stopped and the decrease of the backscattered intensity (I) as a function of the time (T) was observed during 2 minutes, reflecting the process of spontaneous RBC aggregation. Then at the effective shear velocity $\dot{\gamma}$ varying from ~2.5 s^{-1} to ~130 s^{-1} the hydrodynamic stability of RBC aggregates was tested. The dependences I(T) and I($\dot{\gamma}$) were rectified in semilogarithmic coordinates. The characteristic times, which characterized a duration of the first and the second phase of RBC aggregation, were calculated using the formula $t_{1,2}$ = T / ln I. The parameter A defined as the difference between the initial value of I, corresponding to full disaggregation of cells, and the one in the end of the aggregation process, was used to characterize the degree of RBC aggregation as well as the effective size of the aggregates. The indexes of hydrodynamic strength of the bulk of aggregates and the smallest ones were calculated using the formula $\beta_{1,2}$ = $\dot{\gamma}$ / ln I. Additionally, we used the index of strength for the largest aggregates $I_{2.5}$, defined as the percentage of aggregates, disaggregated at the minimal value of $\dot{\gamma}$ ≈ 2.5 s^{-1}. The value of $I_{2.5}$ is taken with a negative sign to make it an indicator of erythrocytes interaction strength rather than that of disaggregation easiness [15]. To characterize RBC deformability we determined the threshold shear velocity $\dot{\gamma}_b$, at which the cell deformation process began in the shear flow. Besides that, we used the indicator tg α, reflecting the degree of erythrocyte deformation in the accelerating flow ($\dot{\gamma}$ changed stepwise from 0 to ~2700 s^{-1}). This indicator characterized a slope of the straight line ID(ln $\dot{\gamma}$), where ID was the deformability index, i.e., the $\dot{\gamma}$-dependent difference between the maximal and minimal diameter of the light ellipse, occurring as a result of the diffraction of laser beam by the cells and corresponding to the shape of an averaged erythrocyte, divided by the sum of these diameters. The maximal elongation of the cells was characterized by IDmax, determined at the maximal $\dot{\gamma}$ ≈ 2700 s-1 [16].

2.3 Modification of fibrinogen-RBC binding

The receptor binding of fibrinogen was affected by monafram, the inhibitor of the glycoprotein GP IIb/IIIa receptors, produced in the Russian Cardiology Research and Production Complex of Moscow. Since under the conditions of our experiment, no practical activation of platelets occurred and the inhibitor affected mainly the erythrocyte receptors [11], we used the samples of whole blood, divided into two parts. To one part (the control one) we added saline (10 μl per 1 ml of blood), and the second one was incubated with monafram (20 mg/ml) during 30 min. Both portions were tested in random order.

2.4 Miscellaneous techniques

The hematocrit was determined by means of microcentrifuging (7000 turns/min., 6 min.; C-702, Apel, Japan). The viscosity of blood plasma was tested by means of the capillary viscometer (the inner diameter of the vertical capillary 0.6 mm, the length 120 mm; ReoMedLab Ltd., Russia). The shape of the cells was monitored using the microscope (40×; Biolam M-1; AO LOMO, Russia).

2.5 Statistical analysis

The data were statistically processed using the software package SPSS 11.5. The data distribution was assessed by means of the Shapiro-Wilk statistics. The significance of the difference between the data obtained in the patients and in the normal subjects was assessed using the unpaired Student t-criterion or the Mann-Whitney criterion. To assess the differences between the control data and the data obtained after the incubation of blood with monafram we used the paired Student t-criterion or the Wilcoxon criterion. The correlation relation was characterized using the Spearman statistics.

For all statistical comparisons, p-value < 0.05 was considered statistically significant. The data are presented as mean value ± standard deviation (SD).

3 Results and discussion

The RBCs of the examined patients with the type-1 or type-2 diabetes mellitus (DM1 and DM2) held the normal shape. Upon the average, no anomalies of hematocrit and blood plasma viscosity were observed in the DM1 and DM2 groups in comparison with the corresponding control groups (N1 and N2). Analogous difference between the groups DM1 and DM2, as well as between the groups N1 and N2 were also not significant (see Table 1).

Table 1 General characteristics of patients with the type-1 (DM1) and type-2 (DM2) diabetes mellitus and healthy volunteers of the corresponding control groups (N1 and N2), as well as hematocrit (Hct) and blood plasma viscosity (η_{pl}).

	Age (years) and number of people (n)	**Hct**	**η_{pl}, mPa•s**
DM1	29.8±9.4, n=20 (7 men and 13 women)	0.40±0.04	1.58±0.17
N1	27.4±5.5, n=113 (40 men and 73 women)	0.41±0.04	1.55±0.30
DM2	60.4±7.6^, n=15 (1 man and 14 women)	0.39±0.04	1.64±0.19
N2	56.0±13.8^, n=11 (1 man and 10 women)	0.41±0.03	1.62±0.20

Note: ^ $p < 0.001$, the comparison of DM1 and DM2, as well as N1 and N2.

Table 2 Characteristic time of the first and the second phase of RBC red aggregation (t_1 and t_2), the effective size of aggregates (A), and the indexes of hydrodynamic strength for large aggregates ($I_{2.5}$) and aggregates in bulk (β_1) in type-1 and type-2 diabetes mellitus patients (DM1 and DM2) and in normal subjects, (N1 and N2, respectively).

	t_1, s	**t_2, s**	**A, rel. units**	**$I_{2.5}$, %**	**b_1, s^{-1}**
DM1	7.83±1.74*	37.4±3.7**	1330±435	-20.1±4.1*	34.1±8.8**
N1	9.72±3.60	34.4±3.7	1239±502	-23.5±7.3	28.5±12.7
DM2	6.39±1.27^^	38.6±3.6**	1470±250^	-17.7±4.7	34.8±11.2
N2	7.75±3.51^	31.3±9.4	1406±567	-21.6±9.9	30.6±10.1

Note: * $p < 0.01$, ** $p < 0.005$, the comparison of DM1 and DM2, as well as of N1 and N2.

3.1 RBC aggregation dynamics in patients with type-1 or type-2 diabetes mellitus

Both in the presence of the disease and in the normal condition, the known age trends [17] of erythrocyte aggregation enhancement and disaggregation process weakening were found to manifest themselves (compare DM1 and DM2, as well as N1 and N2 in Table 2).

Compared to the corresponding groups of normal subjects, in the case of DM1 and DM2 we observed the signs of "hyperaggregation" (see Table 2) that were more clearly seen in the case of DM1, probably, due to the greater number of members in the appropriate group of the tested patients. The intensification of RBC aggregation for both DM1 and DM2 was noticed earlier [18]. However, the detailed analysis of the dynamics of this process revealed an intriguing feature, namely, for both DM1 and DM2, the pathological reduction of t_1, the time of the first phase of RBC aggregation was accompanied by the prolongation of t_2, the second phase time (Table 2). The resulting aggregates possessed increased stability, which was explicitly observed in the case of DM1 and as a trend ($p < 0.06$) in the case of DM2 ($I_{2.5}$ and β_1, Table 2). In the normal state, the disaggregation of cells mainly occurred as a single process, and only in 37% of cases the disintegration of the smallest aggregates was hindered and $\beta_2 = 56.1 \pm 21.8\ s^{-1}$ was recorded. In the DM1 and DM2 groups, β_2 was recorded in 100% of the cases,

Table 3 Monafram-related alterations (M) of the characteristic time of the 1-st phase of RBC aggregation (t_1) and the indexes of hydrodynamic strength for largest aggregates ($I_{2.5}$) and aggregates in bulk (β_1) in the presence of "hyperaggregation" for the type-1 and type-2 diabetes mellitus (DM1h and DM2h) and in the normal state (Nh).

		t_1, c	**$I_{2.5}$, %**	**b_1, s^{-1}**
Nh	control	8.99±3.61	-14.5±5.7	44.0±10.4
	M	10.06±3.49$^{\&}$	-19.2±7.4$^{\&\&\&}$	35.3±10.9$^{\&\&}$
DM1h	control	7.26±0.90	-17.1±2.1	40.3±6.9
	M	7.67±1.01$^{\&}$	-19.0±2.2$^{\&}$	38.5±5.8
DM2h	control	6.45±0.75	-17.6±2.9	47.4±14.0
	M	7.01±1.01$^{\&}$	-19.0±6.6$^{\&}$	39.3±12.6$^{\&}$

Note: $^{\&}$ $p < 0.05$, $^{\&\&}$ $p < 0.01$, $^{\&\&\&}$ $p < 0.005$, comparison of «M» and «control ».

Table 4 Threshold effective shear velocity, corresponding to the beginning of RBC deformation ($\dot{\gamma}_b$), as well as the indice of cells deformation degree in the accelerating flow (tg α) and the index of its maximal deformation (ID_{max}) in the case of type-1 and type-2 diabetes mellitus (DM1 and DM2) and in the normal state (N1 and N2), respectively.

	$\dot{\gamma}_b$, s^{-1}	tg α	ID_{max}
DM1	30.2±46.5^	0.0813±0.0163	0.456±0.019*
N1	19.1±19.6	0.0819±0.0748	0.426±0.042
DM2	12.8±4.5*	0.0773±0.0376	0.456±0.018*
N2	23.2±10.5	0.0742±0.0140	0.399±0.035

Note: * $p < 0.005$, the comparison of "DM1" and "N1", as well as "DM2" and "N2"; ^ $p < 0.05$, the comparison of "DM1" and "DM2".

amounting to 53.8 ± 12.4 s^{-1} and 64.3 ± 11.0 s^{-1}, respectively ($p < 0.01$, the comparison of DM1 and DM2). Thus, for the diabetes mellitus of both types the interaction of erythrocytes at first was accelerated and then abnormally decelerated, resulting in the appearance of the aggregates with increased stability.

3.2 Effect of monafram on the processes of RBC aggregation in patients with the type-1 or type-2 diabetes mellitus

Monafram had no visible effect on the indexes t_2 and A. Generally, in the normal state (n = 31) the only essential effect of monafam was the deceleration of the first stage of erythrocyte aggregation that manifested itself as the increase of the aggregation time t1 from 11.0 ± 4.0 s to 12.9 ± 5.3 s ($p < 0.001$). In the presence of the disease, monafram had an analogous effect. The background and the post-injection values of t_1 amounted to 7.9 ± 1.7 s and 8.3 ± 2.0 s ($p < 0.01$) in the DM1 group (n = 19), 6.5 ± 1.3 s and 6.7 ± 1.2 s in the DM2 group (n = 12), respectively. The averaged indexes of the aggregate stability in all cases demonstrated only an insignificant decrease trend under the effect of monafram, although this trend was sufficiently greater expressed in the patients with DM2, in which the strength index for the smallest aggregates decreased from 60.2 ± 14.9 s^{-1} to 49.9 ± 14.1 s^{-1} ($p < 0.07$).

We divided each of the groups into subgroups in correspondence with the earlier developed criterion [19]: the indices of RBC aggregationand disaggregation being within 95% confidence interval for their normal values, which is a sign of normal aggregation (Nn, n = 19; DM1n, n = 8; DM2n, n = 5), or beyond these limits, which is a sign of "hyperaggregation" (Nh, n = 12; DM1h, n = 11; DM2h, n = 7). The analysis revealed that in the case of normal aggregation-disaggregation dynamics monafram still affected only t_1, increasing it in all subgroups by 5%-20%. In the subgroups with "hyperaggregation" (see Table 3), monafram decelerated the erythrocytes aggregation (t_1) and, additionally, slightly reduced the stability of the aggregates ($I_{2.5}$, β_1) both in the normal state and in the case of disease.

The data on the effect of monafram on the erythrocytes in healthy persons agreed with the analogous data obtained by us earlier. These data showed that the specific fibrinogen-RBC binding only slightly accelerated the cell interaction, which could facilitate the appearance of positive consequences of the normally reversible red blood cells aggregation. On the contrary, in the case of "hyperaggregation" (as a rule, transitory in the normal state) the specific interaction of fibrinogen with the RBC membrane could facilitate abnormal phenomena, related to the accelerated formation of cell aggregates having increased stability [11, 19].

In the case of the diabetes mellitus of both types, the influence of monafram on erythrocytes was similar to that in the normal state, which did not allow us to state a particular role of the specific mechanism in the RBC aggregation for this disease.

3.3 Shear-induced RBC deformation in patients with type-1 or type-2 diabetes mellitus

No possible abnormalities of the RBC deformation manifested themselves under the conditions of accelerated shear flow in the examined patients, suffering from DM of both types (see tg α, Table 4). Moreover, the increase of the deformation-beginning threshold was combined with greater cell stretching in the accelerating flow: the coefficient of correlation between $\dot{\gamma}_b$ and tg α, ρ amounted to 0.48 ($p < 0.05$) in the DM1 group and 0.67 ($p < 0.005$) in the DM2 group. Analogous correlations were found in the normal group N1 ($\rho = 0.39$, $p < 0.001$) and, to a greater degree, in the group N2 ($\rho = 0.72$, $p < 0.005$). The increased index of the maximal erythrocyte stretching, unexpectedly discovered in the studied patients (ID_{max}, Table 3), increased in the DM2 group in the process of the disease (the coefficient of the correlation between the disease duration and ID_{max}, ρ amounted to 0.55, $p < 0.05$). The increased index of cells maximal stretching, as well as the increased degree of their deformation in the accelerating flow in the case of increased deformation

threshold indicated the resistance to the possible aggravation of hemorheological properties in the group of the examined patients.

The division of DM1 patients into 2 subgroups, in which $\dot{\gamma}_b$ was greater (DM1_1, n = 6) and smaller (DM1_2, n = 14) than the upper boundary of the 95% confidence interval for its normal values (i.e., ~23 s^{-1}), and the utilization of data of the standard laboratory testing revealed that the subgroup DM1_1 differed from DM1_2 by narrower diameter distribution of erythrocytes (11.7 ± 0.8% and 14.1 ± 6.4%, $p < 0.05$, respectively) and higher content of triglycerides in the blood plasma (0.91 ± 0.28 mmol/l and 0.66 ± 0.14 mmol/l, $p < 0.05$, respectively), which could partially explain the increased cell deformation threshold in the subgroup DM1_1. Generally, in spite of the factors fortunate for decreasing the erythrocyte deformability and the fact that in DM this decrease was reported in the literature [4, 20] the data obtained by us manifested the compensatory changes rather than the pathological ones at this level.

4 Conclusion

In patients suffering from type-1 or type-2 diabetes mellitus we found the accelerated first phase of erythrocytes aggregation, followed by the anomalously decelerated second phase of the process. In contrast to the normal state, in which the disintegration of the aggregates having different size frequently occurs with equal easiness, in the case of diseases, alongside with the general enhancement of the hydrodynamic strength of aggregates, the stability of the smallest ones grows particularly. The specific component of RBC aggregation mechanisms has no particular significance in the case of diabetes mellitus.

The deformation properties of erythrocytes in the case DM can change ambiguously and, alongside with the increase of the threshold effort required to initiate the deformation, the stretching of erythrocytes in the shear flow can increase, too.

The authors thank Prof. A.V. Mazurov (Russian Cardiologic Research and Production Complex, Moscow) for providing them with monafram and the staff members of the M.F. Vladimirsky Moscow Regional Research and Clinical Institute (MONIKI) for the execution of standard clinical and laboratory examination of the tested persons.

Disclosures

All authors declare that there is no conflict of interests in this paper.

Acknowledgment

The work was partially supported by the Russian Scientific Foundation, grant No. 14-15-00602.

Spatial Poincaré Plots as Descriptors of Speckle Pattern Second-Order Statistics

Anindya Majumdar, and Sean J. Kirkpatrick*
Department of Biomedical Engineering, Michigan Technological University, Houghton, MI 49931, USA

* **e-mail:** sjkirkpa@mtu.edu

Abstract. It is demonstrated herein that the use of spatial Poincaré plots provides an efficient means to describe short and long-range correlations in the spatial structure of the measured intensity distribution of scattered coherent fields. The intensity distribution over a row of pixels in single frames of speckle fields with varying speckle sizes was considered. Statistical descriptors from the spatial Poincaré plots for these intensity data with variable lags were used to estimate the short and long-term variations in the measured intensities, and from these descriptors, the minimum speckle size in the speckle patterns was estimated. This approach yielded similar results for speckle size estimates as the more standard method of calculating the power spectral density of the intensity pattern and simultaneously provided information on the relative contributions of short-term and long-term variations in the measured intensity to the spatial structure of the scattered fields.

Keywords: coherence optics; statistical optics; speckle; Fourier optics; signal processing; speckle imaging.

Paper #3231 received 12 Jul 2017; revised manuscript received 19 Sep 2017; accepted for publication 19 Sep 2017; published online 30 Sep 2017. doi: 10.18287/JBPE17.03.030501.

References

1. J. C. Dainty (Ed.), Laser Speckle and Related Phenomena, 2nd edition, Springer Verlag (1984).
2. X. Zhao, and G. Zhao, "Surface roughness measurement using spatial-average analysis of objective speckle pattern in specular direction," Optics and Lasers in Engineering 47(11), 1307-1316 (2009).
3. R. Jones, and C. Wykes, Holographic and Speckle Metrology, 2nd edition, Cambridge University Press (1989).
4. A. F. Fercher, and J. D. Briers, "Flow visualization by means of single-exposure speckle photography," Optics Communications 37(5), 326-330 (1981).
5. Y. Aizu, and T. Asakura, "Coherent optical techniques for diagnostics of retinal blood flow," Journal of Biomedical Optics 4(1), 61-75 (1999).
6. P. Li, S. Ni, L. Zhang, S. Zeng, and Q. Luo, "Imaging cerebral blood flow through the intact rat skull with temporal laser speckle imaging," Optics Letters 31(12), 1824-1826 (2006).
7. J. C. Ramirez-San-Juan, R. Ramos-Garcia, I. Guizar-Iturbide, G. Martinez-Niconoff, and B. Choi, "Impact of velocity distribution assumptions on simplified laser speckle imaging equation," Optics Express 16(5), 3197-3203 (2008).
8. K. Khaksari, and S. J. Kirkpatrick, "Laser speckle contrast imaging is sensitive to advective flux," Journal of Biomedical Optics 21(7), 076001 (2016).
9. J. W. Goodman (Ed.), Speckle Phenomena in Optics: Theory and Applications, Roberts & Company, Englewood, CO (2007). ISBN 0-9747077-9-1.
10. S. J. Kirkpatrick, D. D. Duncan, and E. M. Wells-Gray, "Detrimental effects of speckle-pixel matching in laser speckle contrast imaging," Optics Letters 33(24), 2886-2888 (2008).
11. K. Khaksari, and S. J. Kirkpatrick, "Combined effects of scattering and absorption on laser speckle contrast imaging," Journal of Biomedical Optics 21(7), 076002 (2016).

12. M. Brennan, M. Palaniswami, and P. Kamen, "Distortion properties of the interval spectrum of IPFM generated heartbeats for heart rate variability analysis," IEEE Transactions on Biomedical Engineering 48(11), 1251-1264 (2001).
13. D. D. Duncan, and S. J. Kirkpatrick, "The copula a tool for simulating speckle dynamics," Journal of the Optical Society of America A 25(1), 231-237 (2008).

Laser speckle patterns are obtained as a result of the random interference of coherent light scattering from a rough surface or a scattering volume [1]. Speckle patterns have been used extensively for a variety of metrology applications including surface roughness [2], strain measurement [3] and fluid flow [4-8]. The second-order statistics of a speckle pattern provide a description of the spatial structure of the pattern, with the minimum size of a speckle, or the minimum correlation length of the pattern, being an important parameter in the characterization of this structure [9]. It has been noted in the literature that proper spatial sampling of the intensity of the scattered field is an important experimental consideration in speckle-based metrology applications [10]. In order to meet the spatial Nyquist criteria, the minimum speckle size of the measured intensity pattern should be at least two pixels [8]. Goodman [9] introduced the *M* parameter which can be interpreted as the number of speckles per pixel and may be used as a means of quantifying this. In practice, the minimum speckle size has traditionally been estimated in two dimensions in terms of the width of the power spectral density (PSD) function of the measured intensity distribution [9]

$$PSD = |\Im\{I(x,y)\}|^2, \tag{1}$$

where $\Im$ represents the Fourier Transform operator and $I(x,y)$ is the distribution of the measured intensity of the speckle field. The typical plot of the PSD function is shown in Fig. 1. The minimum speckle size, Λ, is estimated from this distribution as [8,11]

$$\Lambda = \frac{2D}{W_{PSD}}, \tag{2}$$

where D is the width of the speckle image and W_{PSD} is the width of the PSD function [9]. Note that the PSD is simply the Fourier transform of the autocorrelation function and as such is a measure of the correlation length in the speckle pattern.

A Poincaré plot is a statistical tool to study variations, or, alternatively, self-similarity in a quantity. In these plots, sequential measures of the quantity of interest are plotted against the previous measures. Thus, the i^{th} measure is plotted against the $(i+1)^{th}$ measure, for i = 1,2...*N*-1, where *N* is the total number of measurements available in the data. In biomedical signal processing, these plots have been used extensively to study heart rate variability over time [12]. Specific standard descriptors *SD*1 and *SD*2 can be obtained from the data. These descriptors are mathematically defined as [12]

$$SD1 = Var\{\frac{1}{\sqrt{2}}X_n - \frac{1}{\sqrt{2}}X_{n+1}\}^{\frac{1}{2}} = \frac{1}{\sqrt{2}}\{Var(X_n - X_{n+1})\}^{\frac{1}{2}};$$
$$SD2 = \left\{2Var(X) - SD1^2\right\}^{\frac{1}{2}}, \tag{3}$$

where X_{n+1} and X_n represent the current and previous measures, respectively and *Var*(*X*) stands for the variance in the measurement of *X*. As can be seen from Eq. (3), *SD*1 is a measure of the standard deviation of the differences in successive data points. This is commonly known as the standard deviation in successive differences in statistics [12]. Thus, the descriptor *SD*1 represents the short-term variations in the data [12]. Also, from the expression for *SD*2, it is noted that this represents the difference between the overall variations in the data, *Var*(*X*), and the variations attributed to short-term differences, *SD*1. Thus, the descriptor *SD*2 effectively represents the long-term variations in the data. By these definitions, the ratio *SD*2/*SD*1 is an indication of the prominence of long-term variations in the data, compared to short-term variations [12]. We have referred to this ratio as the ellipticity *e* of the data. We have chosen this nomenclature, as the descriptors *SD*2 and *SD*1 are the semi-major and semi-minor axes, respectively, of an ellipse commonly used to study information from these plots [12] (Fig. 2).

As demonstrated by Brennan, Palaniswami and Kamen [12], for uncorrelated data, this ratio is unity. The larger the deviation of this ratio is from unity, the greater the correlation among the data points. In our research, we have made use of this ability of the Poincaré plot descriptors to indicate whether or not the intensity in neighboring pixels is correlated, which ultimately reflects the minimum speckle size in the pattern.

In order to take advantage of the ability or Poincaré plots to demonstrate correlation between neighboring data points, the traditional definition of Poincaré plot descriptors were modified for the purposes of this study. Instead of plotting every $(i+1)^{th}$ measurement against the i^{th} measurement, we introduced a coarsing factor k, such that every $(i+k)^{th}$ measurement was plotted against the i^{th} measurement, for i = 1,2,…*N*-*k* , with *N* being the number of data points (pixels) available. In previous publications [12], similar descriptors have been referred to as *lag m* Poincaré descriptors. Thus, similar to Eq. 2, the modified descriptors are defined as

$$SD1_k = Var(\frac{1}{\sqrt{2}} X_n - \frac{1}{\sqrt{2}} X_{n+k})^{\frac{1}{2}};$$
$$SD2_k = \left\{2\, Var(X) - SD1_k^2\right\}^{\frac{1}{2}}. \quad (4)$$

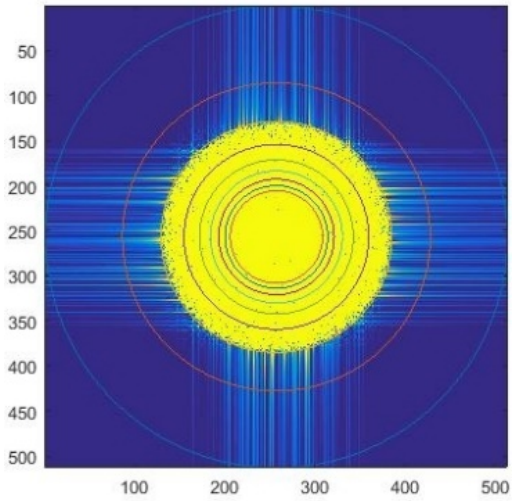

Fig. 1 The Power Spectral Density (PSD) of a frame of 512 × 512 pixels in a speckle field. It can be seen that the PSD width is half the overall width of the field, which in accordance with (1) gives a speckle size of 4 pixels. For easy visualization, concentric circles corresponding to each minimum speckle size from 2 to 10 pixels is drawn on the PSD. The outermost circle corresponds to size = 2 pixels and each subsequent circle inwards corresponds to an increase in size by 1 pixel.

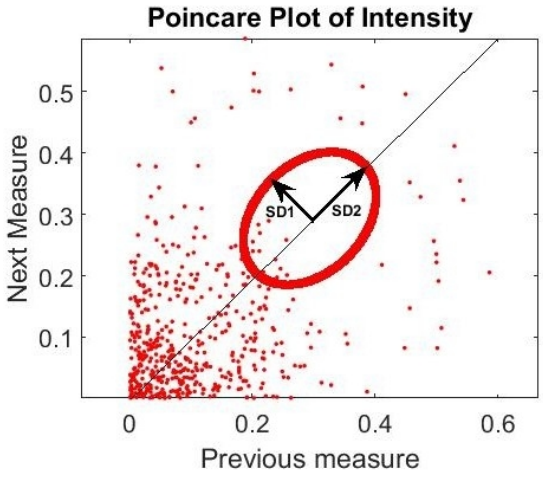

Fig. 2 A typical Poincaré plot. Any particular point represents a data point plotted in vertical axis against the previous data point in the horizontal axis.

Speckle fields were generated using an algorithm as described by Duncan and Kirkpatrick [13]. Using this algorithm, we generated speckle patterns with known minimum speckle sizes varying between 2 and 9 pixels. The intensity distribution of individual rows in these speckle patterns was examined. It has been shown previously [8] that the intensity PSD width accurately gives the minimum speckle size input by the user while implementing this algorithm. Our objective herein was to use modified spatial Poincaré plot descriptors of the intensity distribution along a slice (single row) in the speckle pattern to indicate correlation lengths along this row of speckles and ultimately describe the spatial structure (*i.e,* the minimum speckle size) of the speckle pattern.

The ellipticity e of the obtained intensity distribution was measured for different coarsing factors. In all further discussion, the ellipticity calculated from the data while setting the coarsing factor as k is denoted as e_k. Thus, $e_k = SD2_k / SD1_k$. The ellipticity decreased steadily with an increase in the coarsing factor, until it reached a value approaching unity for all speckle sizes. As mentioned above, this is the point where the distribution is seen to be uncorrelated. By further increasing the coarsing factor beyond this point, the ellipticity exhibited small oscillations, but remained approximately equal to 1.0.

We observed that on steadily increasing the coarsing factor for the calculation of the standard descriptors, the correlation seen in the intensity data was lost when the coarsing factor equals or exceeds the pre-determined minimum speckle size. For example, by examining the case where the minimum speckle size in the simulated speckle pattern was 5 pixels in the data of Fig. 4, it was observed that as long as the coarsing factor was smaller than 5 pixels, the descriptors were able to detect a correlation between the observed intensity values. This results in ellipticity values greater than unity. We refer to this region as the correlated regime. However, when the coarsing factor became larger than 5 pixels, the intensity values detected were seen to be uncorrelated. This resulted in ellipticity values close to unity. We refer to this region as the uncorrelated regime. The minimum speckle size can thus be viewed as the coarsing factor at the transition point between the correlated and uncorrelated regimes.

It is clear from the above discussion that a correlation exists between the minimum speckle size in the speckle pattern and the value of ellipticity at a particular coarsing factor. We observed that for any particular coarsing factor, larger speckle sizes resulted in higher values of ellipticity, unless we are in the uncorrelated regime, in which case $e \approx 1.0$. The characteristic feature of the uncorrelated regime is that the values of ellipticity lie very close to unity and do not continue to decrease monotonically with an increase in coarsing factor. Thus, speckle sizes from multiple speckle fields can be compared by comparing their ellipticity in their intensity distribution, using a low coarsing factor (such as k = 1, which lies in correlated regime irrespective of the speckle size).

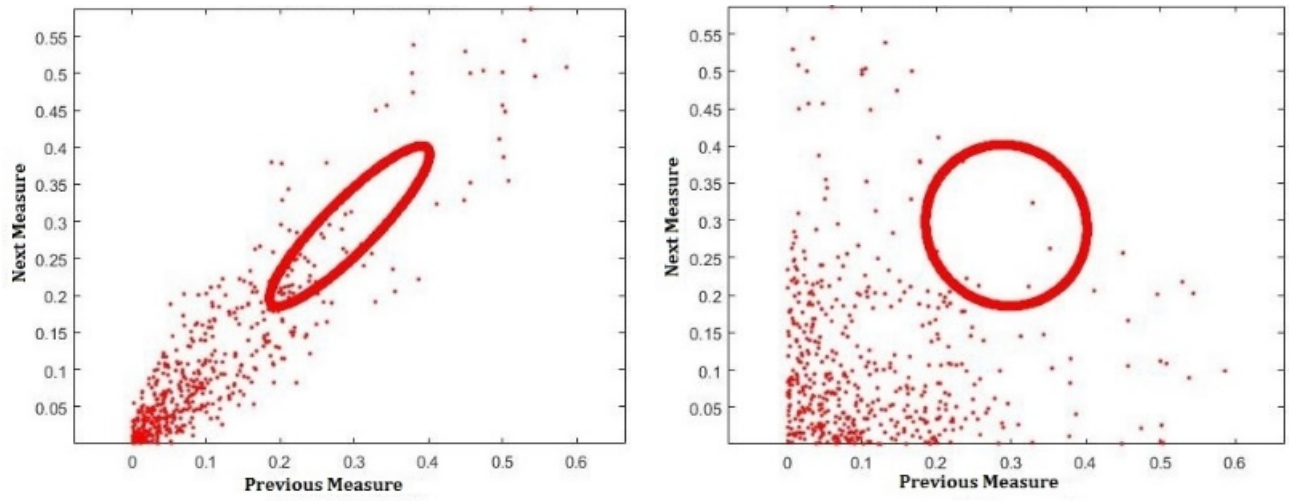

(a) (b)

Fig. 3 Poincaré plot of intensity for minimum speckle size of 5 pixels. (a) When the coarsing factor was 1 pixel, we obtained $SD1 = 0.0344$ and $SD2 = 0.1490$, giving an ellipticity factor of 4.3314 (b) When the coarsing factor was 6 pixels, we obtained $SD1 = 0.1105$ and $SD2 = 0.1058$, giving an ellipticity factor of 0.9575. Thus, the observed correlation is lost at high coarsing factors.

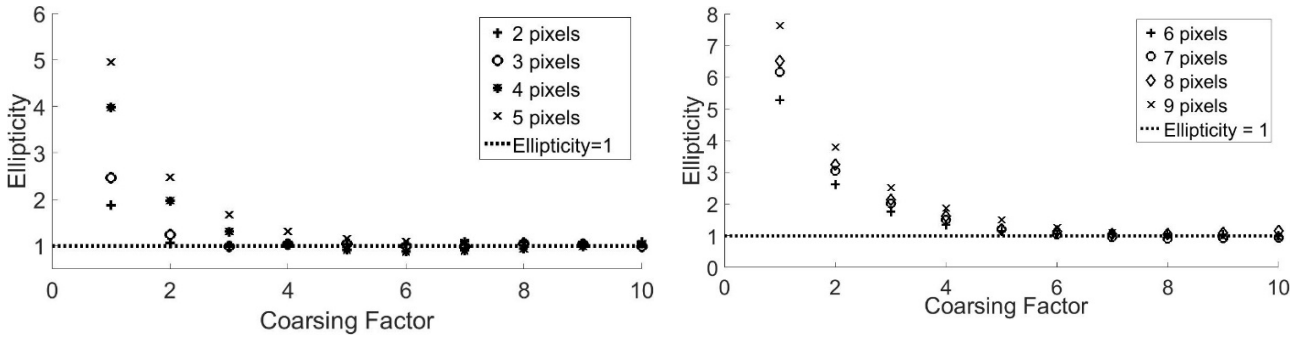

(a) (b)

Fig. 4 Dependence of measured ellipticity on the coarsing factor for minimum speckle sizes of (a) 2 to 5 pixels (b) 6 to 9 pixels. It can be noted that the ellipticity value tends to asymptotically settle around unity, for each of the speckle sizes. We call this asymptotic regime as the uncorrelated regime.

In fact, this ability of the spatial Poincaré plots to distinguish between speckle sizes at low coarsing factors gains significance, especially at larger minimum speckle sizes. Figs. 5(a) and 5(b) demonstrate the challenge with using the PSD for comparing speckle patterns with minimum speckle sizes of 9 and 10 pixels, respectively. According to Eq. (2), the width of the PSD function for the patterns on a 512 × 512 window, are roughly 114 and 102 pixels, respectively. This translates to the radius of the functions to be 57 and 51 pixels. This difference of 6 pixels on a field of 512 × 512 pixels is more challenging to ascertain, compared to the approach using spatial Poincaré plots, as demonstrated in Fig. 5(c).

For a coarsing factor of $k = 1$, which lies in the correlated regime for all speckle sizes greater than 1 pixel, the calculated values of e_k for the speckle patterns of 9 and 10 pixels minimum speckle sizes were 7.63 and 8.41 respectively. For $k = 2$, these values dropped to 3.80 and 4.18, respectively. Thus, for large speckles, calculating the ellipticity value using a coarsing factor of 1 pixel, for example, provides a method of easier comparison than the visual determination of PSD width.

It is worth recalling that the definition of speckle size has a statistical foundation. It is approximated as the square root of the coherence area of the intensity pattern, which is a function of the covariance of the intensity distribution [9]. As the geometry of this coherence is fundamentally two-dimensional, the process of considering its square root only gives an estimate of the one-dimensional *width* of the speckle. For small speckles, the variation of pixel intensity in both dimensions is prominent. As such, defining a boundary between which pixels are to be considered "within the speckle" and which are to be considered "outside" is a relatively straightforward task. However, as the size of the speckles increases, the variation in intensity across the pixels becomes more gradual (*i.e.,* the change extends over more pixels). The stark contrast between neighboring pixels diminishes and thus, the

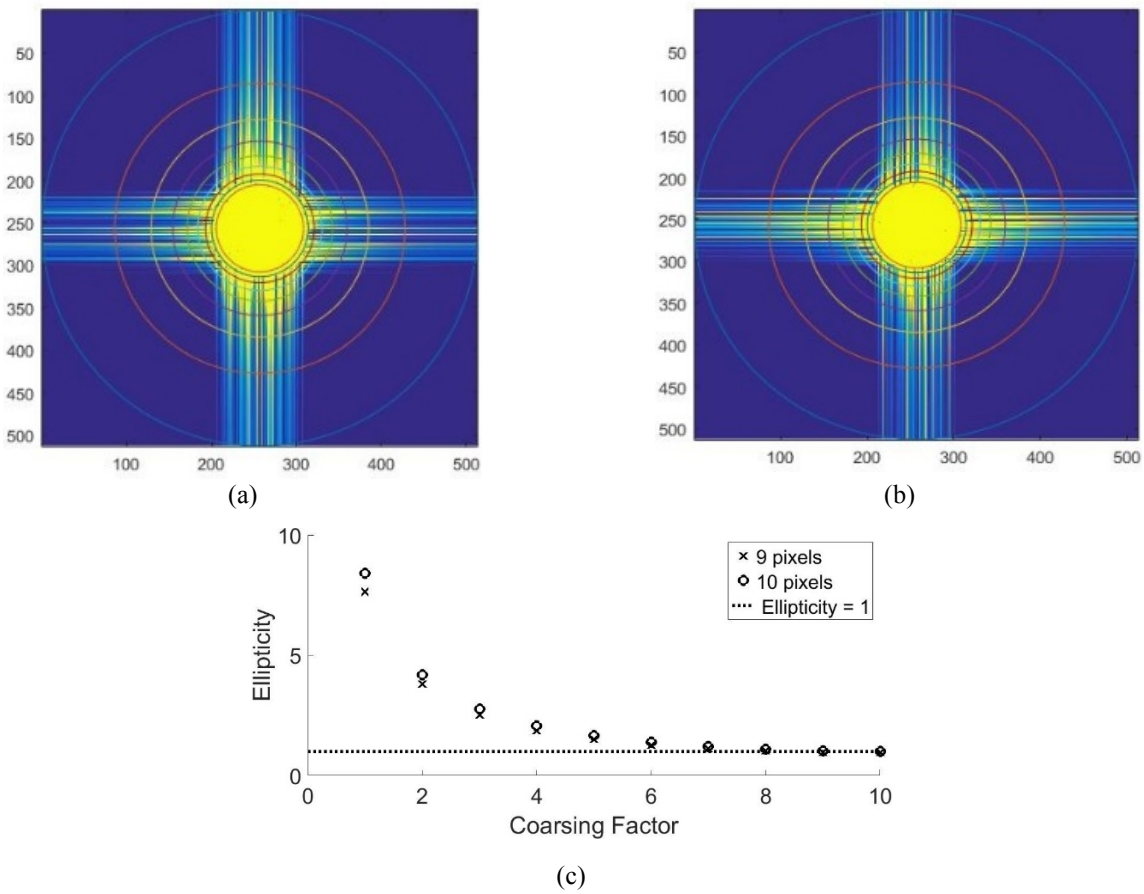

Fig. 5 Comparison of ease of detecting differences in systems with large minimum speckle sizes: PSD for a minimum speckle size of (a) 9 pixels and (b) 10 pixels compared to the (c) ellipticity values for the same minimum speckle sizes.

boundaries between individual speckles becomes spatially less distinct.

In conclusion, the use of modified Poincaré plot descriptors has been demonstrated as an approach for describing the spatial structure in the measured intensity of a speckle pattern. The Poincaré analysis as presented above, provides a useful approach for estimating the minimum speckle size in a speckle pattern. A comparison was made with the results using an alternative approach, that is, the use of the power spectral density function for the calculation of minimum speckle size. The concept of employing a cutoff ellipticity of $e = 1.0$ to identify the minimum sampled speckle size was also introduced. Additionally, it was shown that for large speckles, the present approach has some advantages over the commonly employed approach of assessing the width of the PSD of the speckle pattern. However, at this point the advantages are somewhat qualitative and we have not performed a quantitative assessment of the improvements as this was not the purpose of this study.

Finally, in addition to providing a method for estimating the minimum speckle size in a speckle pattern, spatial Poincaré plots also provide information about the relative contributions of short-term and long-term variations in the spatial structure of the measured intensity distribution of scattered coherent fields.

Disclosures

The authors declare that there are no conflicts of interest related to this article.